

CERN - European Organization for Nuclear Research

LCD-Note-2013-007

CLIC inner detectors cooling simulations

F. Duarte Ramos*, H. Gerwig*, M. Villarejo Bermudez[†]

* *CERN, Switzerland*, [†] *IFIC Valencia, Spain*

December 4, 2013

Abstract

The strict requirements in terms of material budget for the inner region of the CLIC detector concepts require the use of a dry gas for the cooling of the respective sensors. This, in conjunction with the compactness of the inner volumes, poses several challenges for the design of a cooling system that is able to fulfil the required detector specifications. This note introduces a detector cooling strategy using dry air as a coolant and shows the results of computational fluid dynamics simulations used to validate the proposed strategy.

Contents

1. Introduction	3
1.1. Inner Region Layout	3
1.2. Cooling Strategy	6
2. Computational Fluid Dynamics Simulations	10
2.1. Vertex Detector Air Supply	10
2.2. Vertex Detector Volume	14
2.3. Vertex Detector Barrel Submodel	23
2.4. Single Ladder Simulations	36
2.5. Forward Tracking Volume	41
2.6. Model Validation	48
3. Conclusion	51
A. CFD Model characteristics	52
A.1. Convergence criteria	52
A.1.1. Residuals	52
A.1.2. Imbalances	52
A.1.3. Variables	53
A.2. Turbulence	53
A.2.1. Near wall treatment	53
A.3. Boundary Conditions	54

1. Introduction

The inner region of the CLIC detectors concepts (CLIC_SiD and CLIC_ILD), with special emphasis on the vertex detector, must have excellent spatial resolution, full geometrical coverage extending to low polar angles, extremely low mass, low occupancy facilitated by time-tagging, and sufficient heat removal from sensors and readout [1]. These considerations, together with the physics needs and beam structure of CLIC, push the technological requirements to the limits and imply a very different design than the ones currently in use elsewhere. Although the same study can be extended to CLIC_SiD, this note is focused on the development of a cooling strategy for the inner region of the CLIC_ILD detector concept.

Strict requirements are set in terms of material budget for the detectors in the inner region of the CLIC_ILD detector concept, especially for the vertex detector where a goal of 0.40% X/X_0 per double sided layer is set (of which 0.21% correspond to the 200 μm of silicon required for the sensors and readout chips). This puts serious constraints on the amount of material that can be used for support, services and cooling of the detectors.

To fulfil the material budget requirements, solutions can be found using, for example, lightweight materials like carbon fibre reinforced composites or specialized structural foams for the supports, and aluminium cables for power delivery and data transmission. However, the use of conventional liquid/two-phase cooling solutions would result in a significant increase in material budget from both the cooling medium and its tubing. Therefore, the use of a dry gas (air or N_2) as a coolant has been proposed for the inner region detectors as a means to achieve the specified material budget.

This note introduces the proposed cooling strategy and presents a first order validation of the concept through the results of Computational Fluid Dynamic (CFD) simulations of individual control volumes inside the inner region. The note is structured as following: an introduction of the layout of the inner region is followed by the presentation of the cooling strategy; subsequently, the different finite element models used for the validation are described with their results being shown and discussed.

1.1. Inner Region Layout

The CLIC_ILD inner region is composed of a vertex detector and an inner tracker as shown in Figure 1. The current physics simulations foresee that, for the vertex detector, both the three barrel layers as well as the three endcap disks will be composed of double-sided structures that make use of silicon pixel detectors¹⁾. The choice of a double-sided configuration was made to minimize the amount of support material needed and thus help achieve the required material budget (0.40% X/X_0 per double sided layer) as well as mitigate the deformations perpendicular to the silicon planes due to differences in the thermal performances of the multiple materials

¹⁾Additional simulation studies are in progress, comparing detector performances for single and double layers, different amounts of material assumed for the support structure, etc. (see [2, 3]).

within each layer.

The vertex barrel has an inner radius of 31 mm, an outer radius of 60 mm and a half length of 130 mm. As for the vertex endcap disks, their inner radius is 33 mm whilst the outer radius is 102 mm and they are positioned from $z = \pm 160$ mm to $z = \pm 257$ mm.

The silicon inner tracking system of the CLIC ILD detector concept is composed of a two-layer cylindrical Silicon Internal Tracker (SIT)²) and five single-sided Forward Tracking Disks (FTD) as shown in Figure 1a. All these layers make use of silicon micro-strip technology detectors with the exception of the innermost FTD which uses silicon pixel technology. The main tracker (not shown) is composed of a Time Projection Chamber (TPC), complemented by a Silicon External Tracker (SET) and an Endcap Tracking Disk (ETD) layer, both composed of silicon strip detectors.

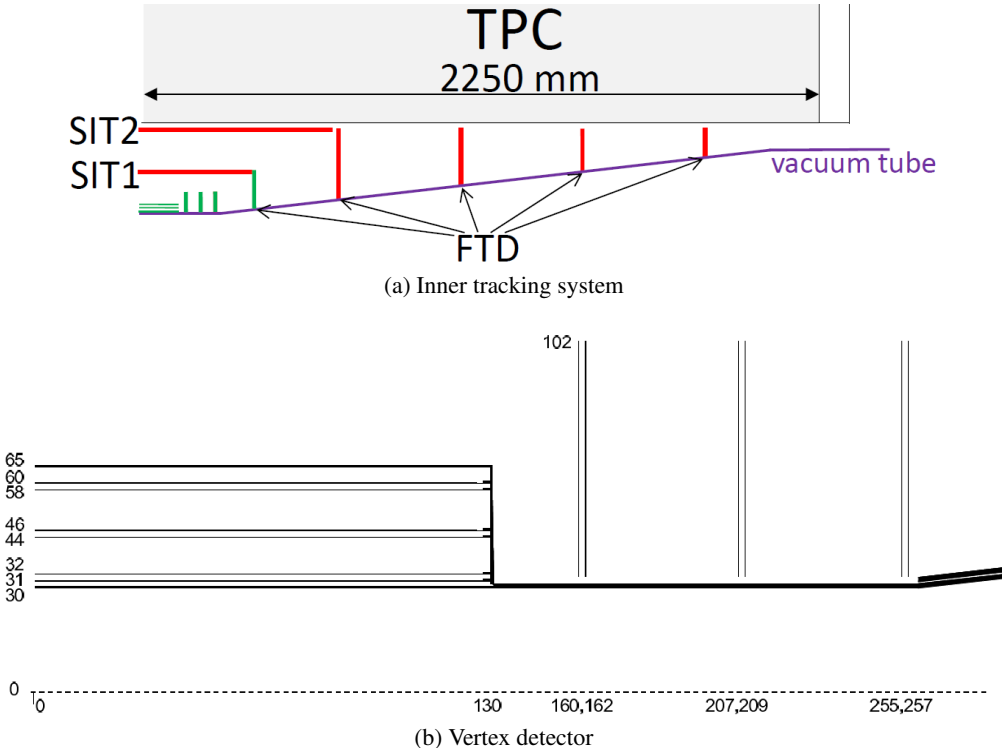


Figure 1: Sketch of the physics layout of the inner region of the CLIC ILD detector concept in the z - r plane (from [1]). Shown are the two silicon micro-strip layers of the inner tracker barrel (SIT1 and SIT2) and the five single sided forward tracking disks (the innermost using silicon pixel technology and the four remaining ones using silicon micro-strip technology) (a) as well as the three double sided silicon pixel layers of the barrel and endcap disks of the vertex detector region (b).

²In the CDR simulation studies, the SIT detectors are implemented as "false double-sided" detectors.

Both the vertex detector and the inner tracker surround a hybrid beam pipe composed of a cylindrical part made of beryllium and two conical stainless steel portions. For the beryllium portion of the beam pipe, a wall thickness of 0.6 mm has been assumed for the CLIC-ILD detector concept. In order to provide shielding against backscattering of background particles from upstream beam and detector elements, the wall thickness of the conical portions is 4 mm. An outer cylinder, split in two halves, made of a carbon fibre reinforced polymer (CFRP) provides the mechanical support and positioning for the detectors of the inner region as well as the beam pipe (see Figure 2).

Due to the fact that the existing detector technologies are not able to simultaneously fulfil all the requirements imposed by the physics goals and the running conditions constraints, the sensor and readout technology for the vertex detector has not yet been chosen. Ongoing R&D studies focus on bump-bonded hybrid pixel detectors with 50 μm thick silicon sensor read out through complex 50 μm thick readout ASICs. Pixel sizes of 25 $\mu\text{m} \times 25 \mu\text{m}$ are foreseen to achieve 3 μm single-point resolution. To reduce dead areas, Through-Silicon Via (TSV) interconnect technology is foreseen, allowing to connect to ASICs and sensors directly perpendicular to the readout planes. Vibration-induced distortions have to be small ($\sim 1 \mu\text{m}$ in-plane amplitude) compared to the single-point resolution. The requirements for alignment precision and temperature-induced distortions are less severe, as they can be corrected for with optical and track-based alignment methods, provided the weak modes are sufficiently constrained.

In order to reduce power consumption, the low accelerator duty cycle (156 ns bunch train and 20 ms repetition period) is used in a power-pulsing scheme of the detector electronics [4, 5]. This scheme is foreseen to allow the power dissipation to be at the level of 50 mW/cm² for the pixel based layers so that the use of air cooling can be possible. The power dissipation for the micro-strip based layers is expected to be significantly lower ($\sim 1 \text{ mW/cm}^2$).

Further details about the physics layout and performance of the CLIC-ILD inner region can be found in [1] and [6]. The work presented in this note concerns the volume occupied by the vertex detector and the inner tracking system.

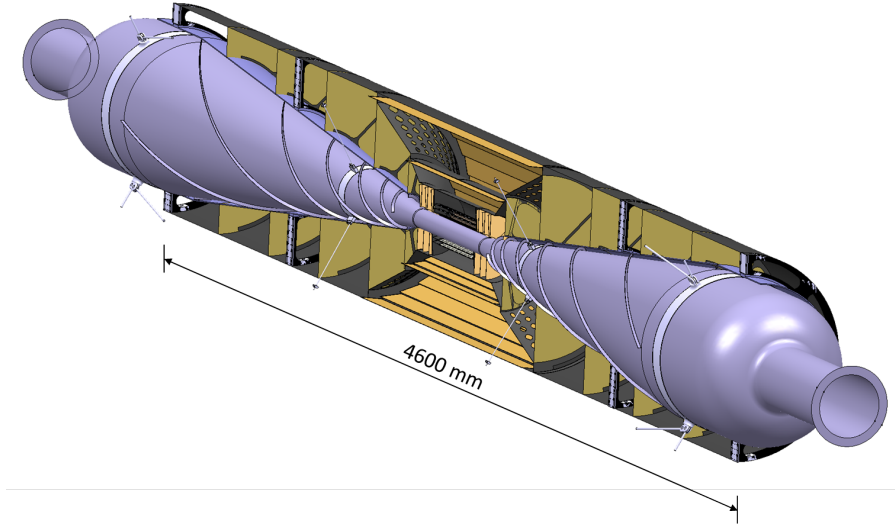


Figure 2: Engineering layout of the CLIC-ILD inner region.

1.2. Cooling Strategy

A dry gas (air or N_2 ³) has been proposed for the cooling of the detectors in the inner region as a means to achieve the strict requirements for the material budget in this volume. One of the main challenges of using gas cooling is to achieve a uniform gas delivery to all detector surfaces whilst minimizing the amount of material in the form of ducts/pipes. A proposed solution for the air delivery inside the inner region of CLIC-ILD consists of having two independent cooling streams inside the volume defined by the cylindrical CFRP support tube (as shown in Figure 3): an outer stream will provide the air necessary to cool the FTDs 2-5 whilst an inner one will serve to cool the vertex detector as well as the SIT and FTD1 layers.

For the outer stream, the air will be provided through openings in the bottom of the CFRP support tube and extracted from openings on the top as shown in Figure 3a. For the supply of the air to the innermost region, a solution has been proposed where the initial design of the beam pipe with 4 mm thick conical walls is modified to become a "double-wall" design. In this proposal, the thickness of the conical portions of the beam pipe is reduced to the minimum value required to satisfy vacuum and load bearing specifications whilst a second stainless steel conical shield is added around the beam pipe conical portions. The thickness of this shield will have to be optimized in a future series of full detector simulations. The gap between the conical shield and the beam pipe serves as the duct needed to supply/extract air to/from the innermost region. This solution has the added benefit of reducing the weight of the beam pipe and thus minimize the loads on the fragile beryllium portion whilst at the same time providing an air duct without increase in material. The introduction of this duct comes at the expense of a slight decrease in

³The thermal behaviour of both gases is similar. For example, at 300 K: $\rho_{air} = 1.161 \text{ kg/m}^3$, $\rho_{N_2} = 1.123 \text{ kg/m}^3$; $c_{p_{air}} = 1.007 \text{ kJ/kg}\cdot\text{K}$, $c_{p_{N_2}} = 1.041 \text{ kJ/kg}\cdot\text{K}$; $k_{air} = 26.3 \cdot 10^{-3} \text{ W/m}\cdot\text{K}$, $k_{N_2} = 25.9 \cdot 10^{-3} \text{ W/m}\cdot\text{K}$.

acceptance (currently, the gap between the conical shield and the beampipe is 10 mm). Figure 3b shows the flow direction inside the innermost region. This arrangement of streams allows the air to be provided to the inner region from one side of the detector and extracted from the opposite, thus simplifying the routing of the cooling related services.

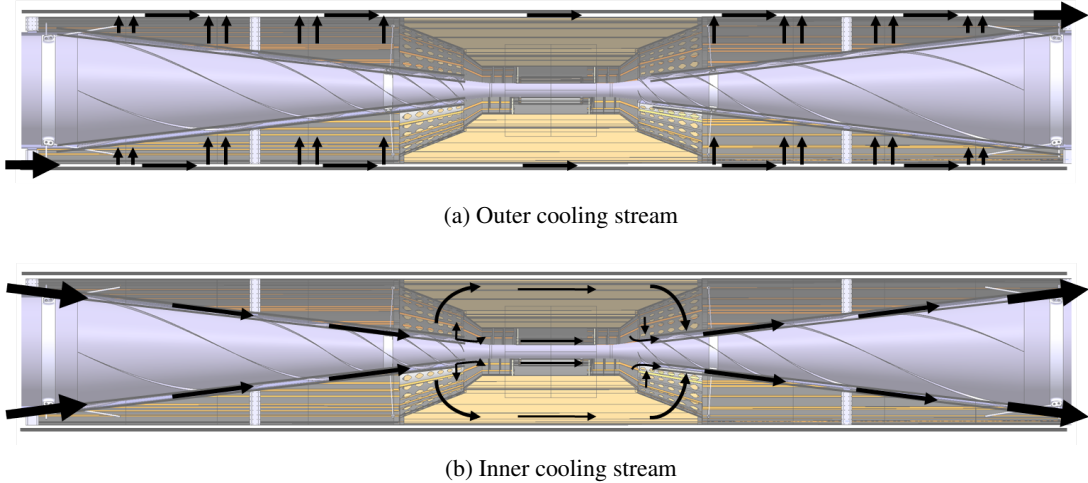


Figure 3: Sketch showing the proposed cooling strategy for the inner region of the CLIC ILD detector concept.

Since the air supply to the innermost region is perpendicular to the vertex detector endcaps, a solution had to be found to properly cool the vertex detector endcaps while minimizing large scale flow disturbances that would increase the pressure drop inside the innermost region and degrade the cooling efficiency. The proposed solution adds a significant tangential component to the air flow inside the vertex detector volume. To match the flow direction, it is proposed to split the three vertex detector endcap disks into twenty-four petals that are distributed around the beam pipe following a helical path with a pitch equal to the initial distance between the vertex endcap disks (see Figure 4). In order to induce the tangential velocity component to the flow entering the vertex detector model, a set of helical shaped deflectors was added to the volume between the conical beam pipe portion and the stainless steel shield as shown in Figure 5a. Once inside the volume of the vertex detector, the air is allowed to flow in between the vertex endcap petals and barrel layers as shown schematically in Figure 5b. The impact on the physics performance of the different layout changes proposed for the air-cooling scheme is being evaluated [2, 3].

Furthermore, in order to also minimize the flow disturbances that could cause unwanted vibrations in the transition between the vertex endcap and the barrel regions, the support structure for the vertex barrel ladders was designed in order to match the flow direction inside the vertex detector volume. To achieve this goal, a CFRP/Rohacell sandwich structure with a helical shape with the same pitch as the one used in the placement of the vertex endcap petals is used to sup-

port the ladders from each side of the barrel as show in Figure 6.

The cooling of both layers of the SIT is achieved through a secondary longitudinal air stream that has its origin in openings on the beam pipe shield near the innermost FTD (see Figure 5b). This cooling strategy is expected to provide a uniform stream of air to all sensor surfaces without adding material for the air delivery in the form of ducts or pipes.

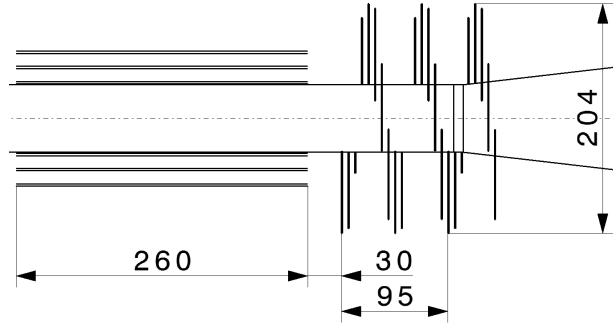
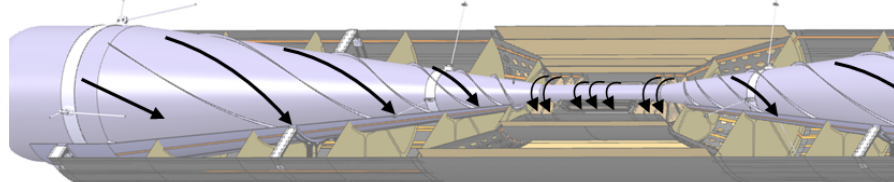
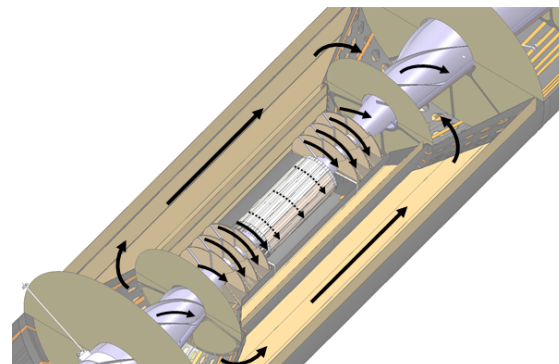


Figure 4: Sketch of the engineering layout of the CLIC ILD vertex detector showing the characteristic dimensions (in millimeters).

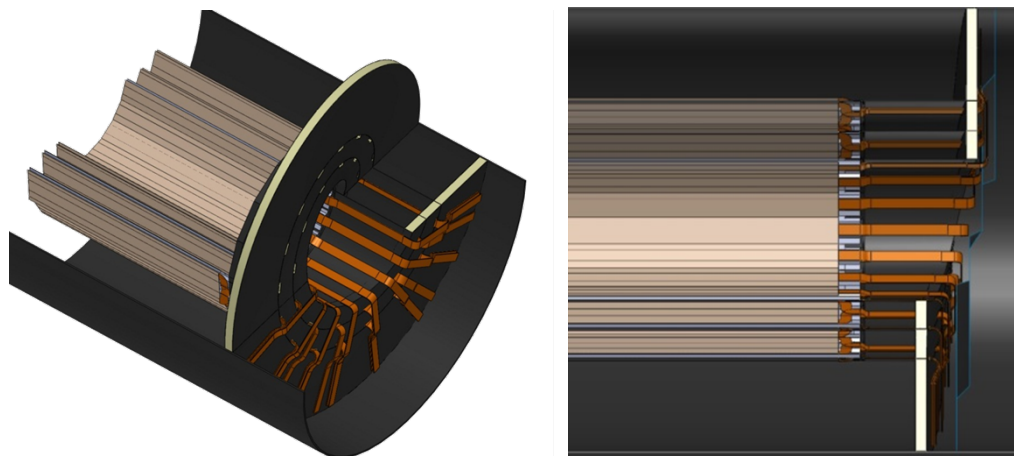


(a) Deflectors are used to induce a tangential component to the velocity vector



(b) Detailed sketch showing the flow within the vertex detector and SIT volume

Figure 5: Sketch showing the proposed cooling strategy for the inner region of the CLIC ILD detector concept.



(a) 3D view of the support structure with only one quarter
of the barrel ladders and services being shown.

(b) Top view

Figure 6: Vertex detector barrel support structure. This CFRP/Rohacell sandwich structure is designed to minimize large scale disturbances in the flow transition between the endcap and barrel regions.

2. Computational Fluid Dynamics Simulations

In order to obtain a first order validation of the proposed cooling strategy, a series of Computational Fluid Dynamics (CFD) models was created for different control volumes within the inner region of CLIC ILD. These models were created and analysed using the commercial CFD software package ANSYS® CFX v14.5. In the following the characteristics and results from each model are presented.

2.1. Vertex Detector Air Supply

As mentioned in §1.2, a set of helical shaped deflectors are placed between the conical portion of the beam pipe and the stainless steel shield to induce the tangential velocity component to the flow entering the vertex detector volume. In order to determine the flow characteristics inside this supply duct and most importantly at the transition to the vertex detector volume, a CFD model of this duct was created. The velocity calculated at the outlet of this model will later be used as a boundary condition for the vertex detector simulation (see §2.2).

Since the current proposal includes four deflectors distributed equally around the beam pipe along the circumferential direction, only $1/4$ of the fluid inside the duct was modelled. The finite element mesh, shown in Figure 7, is composed of both tetrahedral elements for the bulk volume and prisms for the near wall treatment. The typical element size is 4 mm and the total cell count approximately 2.8 millions.

The air was modelled using the "Air at 25° C" material properties available in the ANSYS CFX library with a reference pressure of 1 atm being specified (the material properties are modified internally by the software to account for the applied boundary conditions). The volume was considered to be isothermal with a temperature of 0° C and the turbulence was modelled through the use of a k- ω Shear Stress Transport (SST) model (more details about this model can be found in Annex A). The boundary conditions shown in Table 1 were applied.

Table 1: Boundary conditions applied to the vertex detector air supply model.

Location	Boundary condition
Inlet	Mass flow rate = 5.25 g/s
Outlet	Relative pressure = 0 Pa
beam pipe and shield walls	No slip and smooth wall
Deflectors	No slip and smooth wall

The analysis was defined as steady-state with an auto timescale as well as an RMS residual target of 10^{-4} and a conservation target of 10^{-2} as convergence criteria. As shown in Figure 8, the simulation achieved the convergence targets after 21 iterations, with the average pressure at the inlet achieving steady state conditions after about 10 iterations. The ANSYS CFX manual recommends that, in order to verify the validity of the $k-\omega$ SST turbulence model, a y^+ (variable based on the distance from the wall to the first node and the wall shear stress⁴⁾) inferior to 2 should be globally achieved. Figure 9a shows the y^+ distribution over the solid surfaces of the model with its maximum value being 1.02, which confirms the ability of the mesh/turbulence model to describe the near wall behaviour. A plot of the air streamlines is shown in Figure 9b. For a mass flow rate of 5.25 g/s, the average velocity at the inlet is 1.24 m/s. The corresponding averaged value of the circumferential velocity component at the outlet is 9.7 m/s with the axial one being 5.4 m/s (the average velocity at the outlet it 11.1 m/s). These values will be used for the specification of the boundary conditions of the vertex detector volume model.

The Reynolds number for an internal flow is given by:

$$Re_L = \frac{\rho \cdot V \cdot L}{\mu} \quad (1)$$

where ρ and μ are the fluid's density and dynamic viscosity respectively, V is its velocity and L is a characteristic dimension of the channel. To validate the applicability of the turbulent flow assumption inside a non uniform channel, the average Reynolds number is used with the characteristic dimension being equal to the cubic root of the channel's volume. For this simulation, the average Reynolds number inside the supply duct is 1.56×10^4 , which confirms the turbulent flow assumption. For reference, the calculation of the Reynolds number at any point of the supply duct can be done using a characteristic length equal to the hydraulic diameter:

$$D_h = \frac{4 \cdot A_c}{P} \quad (2)$$

where A_c and P are the flow cross-sectional area and the wetted perimeter, respectively. For the outlet of the supply duct, the Reynolds number is then 1.44×10^4 . For the conditions simulated, the pressure drop inside the supply duct is 113 Pa.

⁴Since the velocity next to a no-slip wall boundary changes rapidly from a value of zero at the wall to the free stream value a short distance away from the wall, a fine enough mesh near a wall would be needed to accurately resolve the velocity profile in the boundary layer. Wall functions can be used in these cases to apply an assumed functional shape of the velocity profile. Therefore, the boundary layer is partially resolved by nodes near the wall and wall functions are used to supplement accuracy where the nodes are not sufficiently clustered near the wall. One indicator of the closeness of the first node to the wall is the dimensionless wall distance y^+ . Its definition is presented in Annex A.

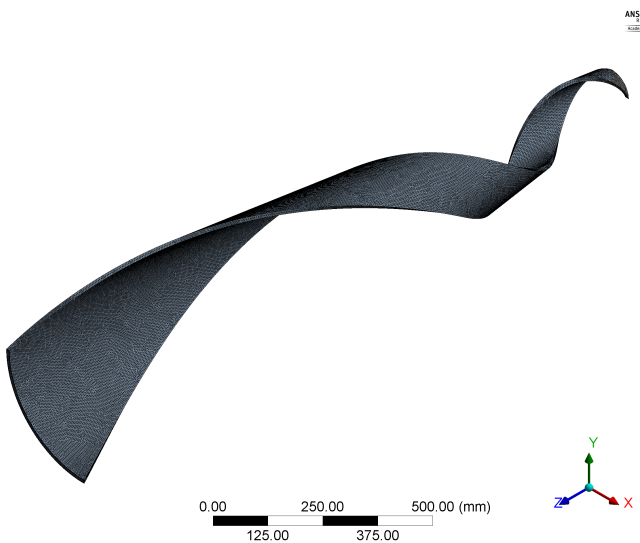


Figure 7: Mesh of the duct.

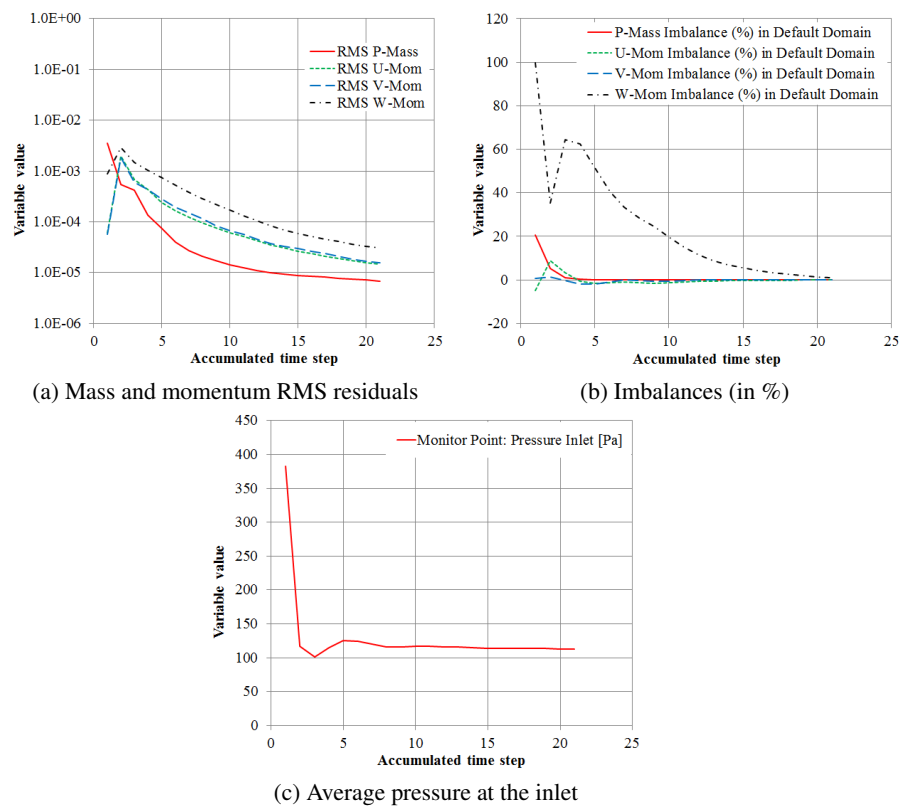
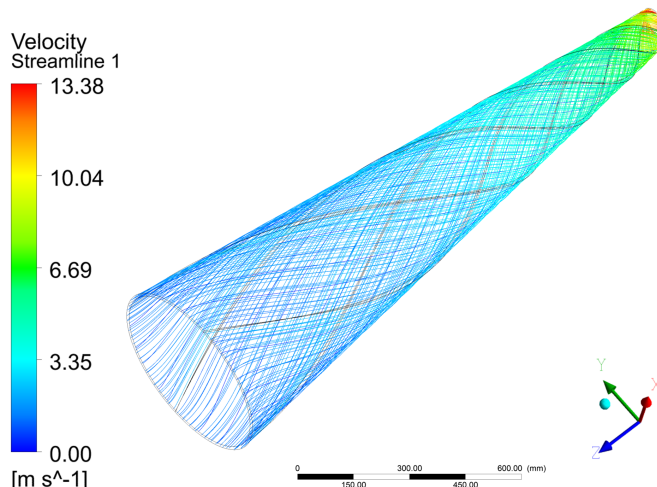
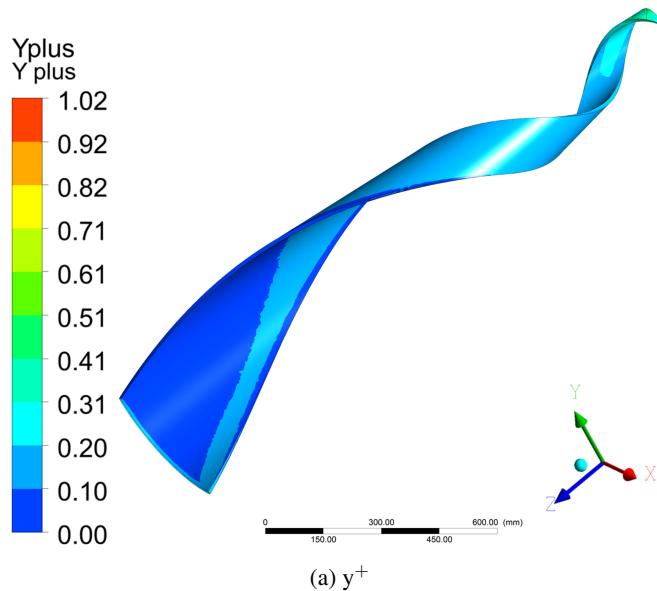


Figure 8: Duct simulation convergence



(b) Velocity streamlines (please note that in the picture a circular pattern was applied to the results to better illustrate the flow behaviour inside the supply duct)

Figure 9: Results of the simulation of the flow conditions inside the conical supply duct.

2.2. Vertex Detector Volume

Once inside the vertex detector volume, the air is intended to cool both the vertex detector endcap petals and barrel ladders in the most uniform way possible. To evaluate the flow characteristics inside this volume, a CFD model of this region was created with the geometry shown in Figure 10. As it was the case of the model presented in §2.1, only the air inside the volume was modelled, with the interfaces between the air and the solid surfaces being modelled as no slip and smooth walls with the appropriate heat flux values. This strategy was adopted in order to simplify the analysis at the expense of only being able to model the heat transfer through convection between the walls and the air. Therefore, no conduction inside the solid materials has been modelled, as well as no heat exchanges through thermal radiation. More detailed analyses will be needed in the future to precisely determine the surface temperature of the solid walls.

The CFD model of the vertex detector is defined by the air that is enclosed inside the vertex detector support tube, the innermost FTDs and the beam pipe as shown in Figure 10a. Each of the 48 endcap petals was modelled using two flat surfaces that are 2 mm apart along the z-axis (where a 50 mW/cm^2 heat flux is applied) and two side surfaces that connect the two parallel surfaces along their radial edges. In order to simplify the model and reduce the number of cells in the mesh, the barrel portion of the vertex detector was modelled through the use of cylindrical surfaces as shown in Figure 10c. In this case, the barrel portion is composed of 6 cylindrical surfaces where a 50 mW/cm^2 heat flux is applied. In order to simulate the double-sided ladder design, the air is only allowed to flow on one side of each surface. A detailed model of the vertex detector barrel is presented in §2.3. The support structure of the barrel ladders was also included in the model with only the surfaces in contact with the air being included. The inlet and outlet of the volume were modelled as annular surfaces with a cross-section that equals the one of the conical duct at the transition to the vertex detector volume (the z-coordinates of the inlet and outlet have negative and positive values respectively, with the origin of the coordinate system being placed at the interaction Point (IP) and the z-axis pointing along the axial direction). Table 2 summarizes the boundary conditions that were applied to this model.

Table 2: Boundary conditions applied to the vertex detector volume model.

Location	Boundary condition
Inlet	Axial velocity = 5.4 m/s; Tangential velocity = 9.7 m/s; Temperature = 0° C; Turbulence intensity = 5% (default value)
Outlet	Relative pressure = 0 Pa
VTX petals	No slip and smooth wall; Heat flux = 500 W/m ²
Barrel layers	No slip and smooth wall; Heat flux = 500 W/m ²
FTD 1	No slip and smooth wall; Heat flux = 250 W/m ²
Remaining surfaces	No slip and smooth wall; Adiabatic

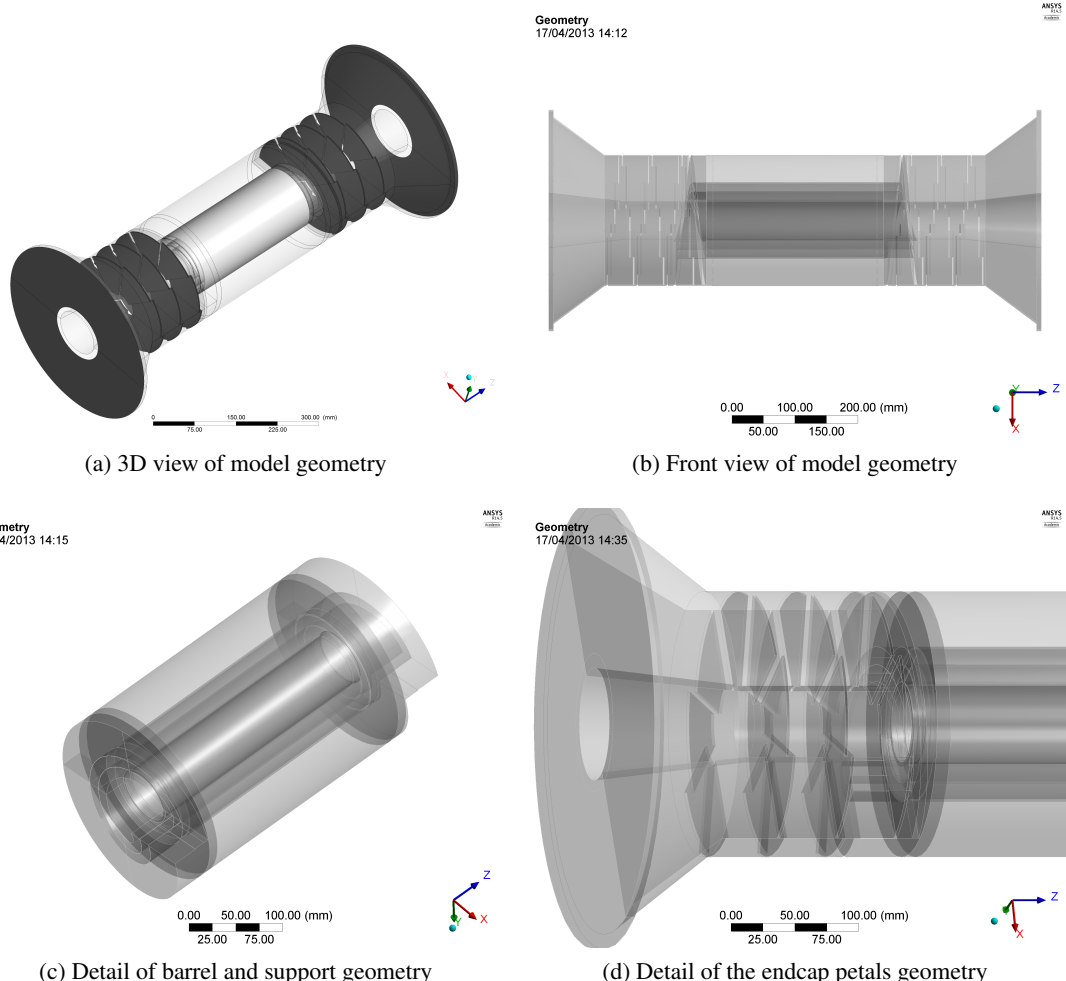


Figure 10: Vertex detector model geometry.

The mesh that was generated for this geometry is shown in Figure 11. In order to simplify the mesh generation process and improve its quality, the geometry was split into several simpler volumes corresponding to the two endcaps regions, the barrel region and the two barrel support structures. In addition, the endcap volumes were further split longitudinally along the z-x plane. The connection of the different sub-meshes was achieved by defining the proper interfaces between the fluid regions (a conservation of mass and energy was specified at the interfaces). The mesh is mostly composed of tetrahedral elements for the bulk volume and prisms for the near wall treatment, with the barrel region being modelled using hexahedral elements. The typical element size is 5 mm, with finer elements (1–2 mm) being employed in areas where finer detail is needed (e.g. in the volume between the beam pipe and the first barrel layer). The total cell count in the mesh is approximately 7 millions.

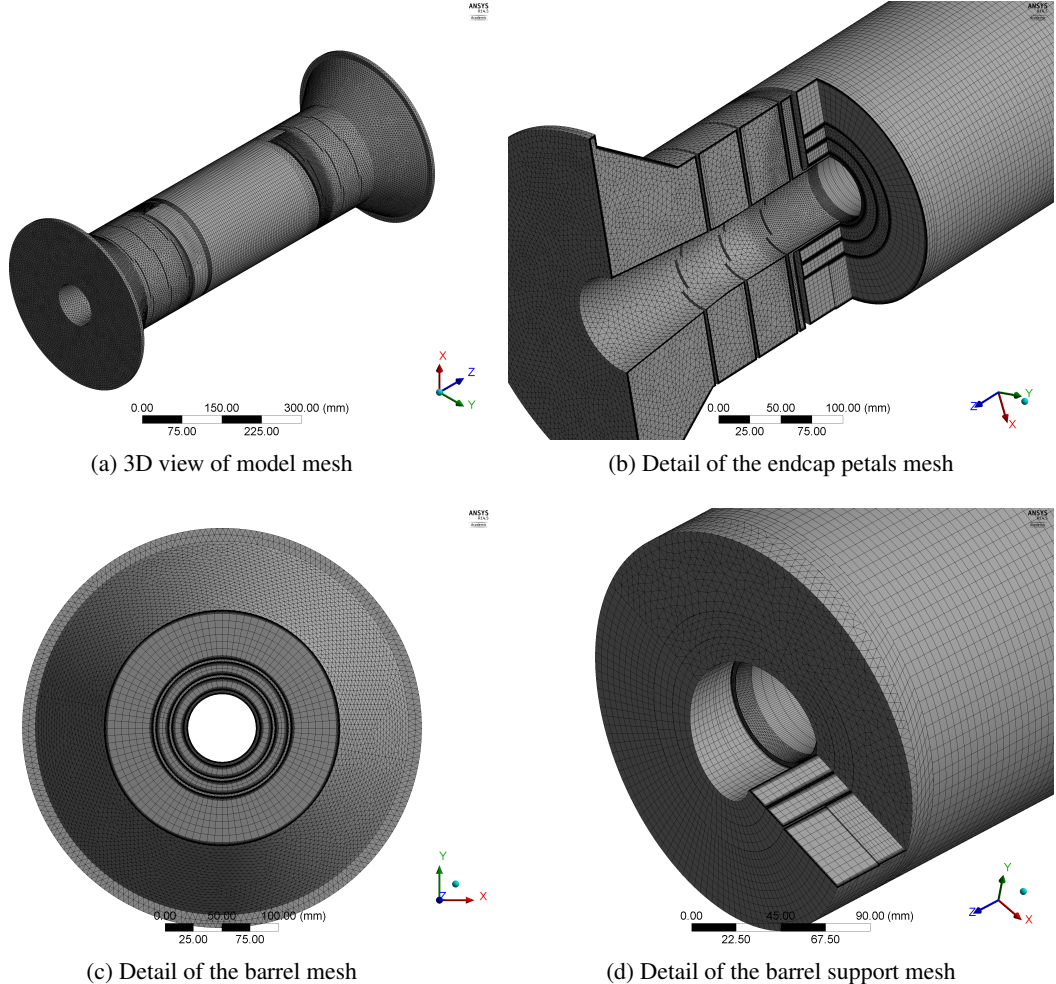


Figure 11: Vertex detector model mesh.

The air was modelled using the "Air at 25° C" material properties available in the ANSYS CFX library with a reference pressure of 1 atm being specified. The simulation of the heat transfer inside the air was achieved using the "Thermal Energy" heat transfer option of ANSYS CFX which, according to its documentation, models the transport of enthalpy through the fluid and is suitable for modelling heat transfer in low-speed flows (i.e. far from supersonic). The turbulence was modelled through the use of a k- ω SST model.

Similar to the model described in §2.1, the analysis was defined as steady-state with an auto timescale as well as an RMS residual target of 10^{-4} and a conservation target of 10^{-2} as convergence criteria. The corresponding convergence plots are shown in Figure 12, with the solving process being interrupted after 2000 iterations. Although neither the residuals nor the imbalances achieved the specified targets, one can observe that after 1000 iterations the variables of interest (average surface temperatures, pressure at the inlet and velocity at the outlet) have

achieved stable values. Since the residuals and the imbalances are close to the specified targets, one can assume that the solution has achieved steady-state conditions.

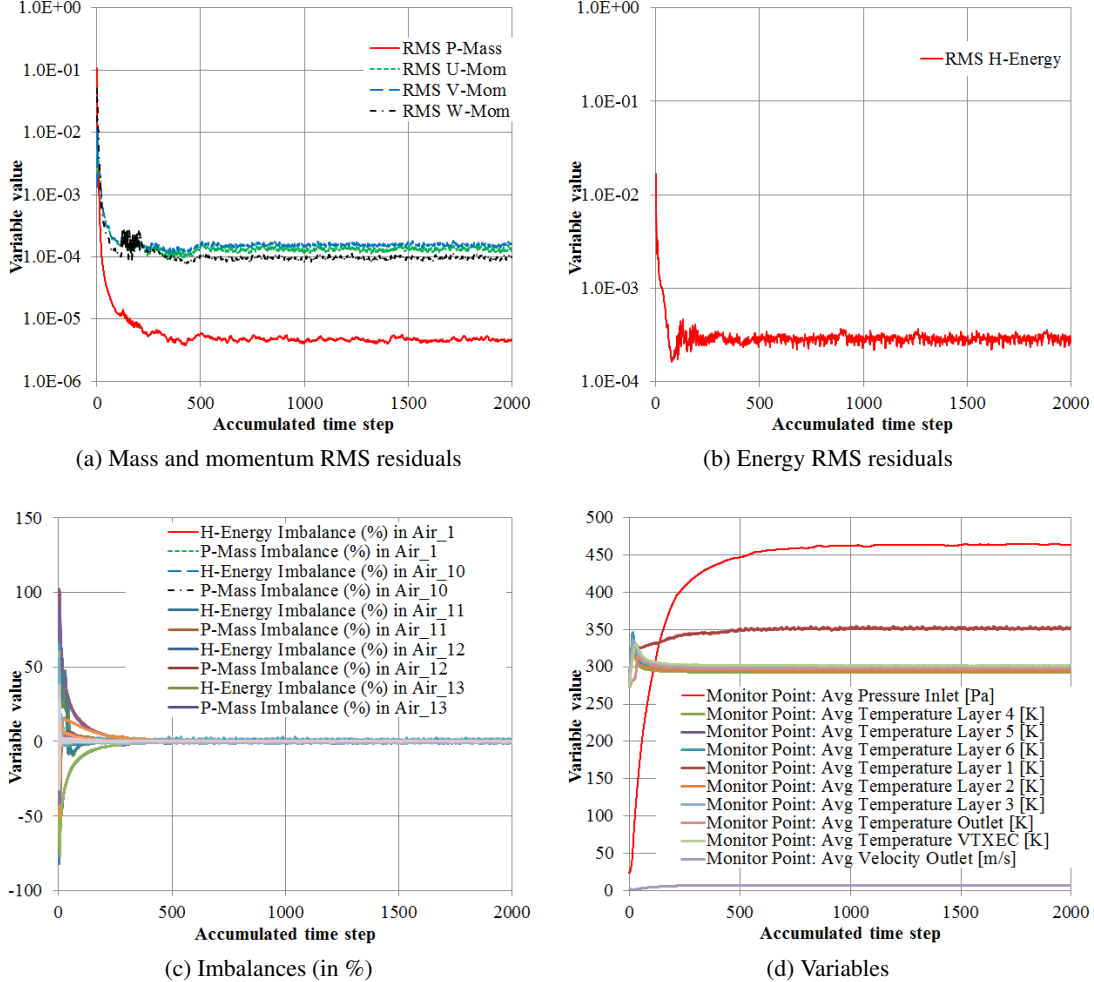


Figure 12: Vertex detector simulation convergence.

The y^+ distribution over the solid surfaces of the model is shown in Figure 13. The results show that the overall values of the y^+ variable are within the recommended range and therefore confirm the ability of the mesh/turbulence model to describe the near wall behaviour of the flow. The average Reynolds numbers in the different sub-volumes range from 4.4×10^3 to 6.0×10^4 which also confirms the assumption of a turbulent flow regime.

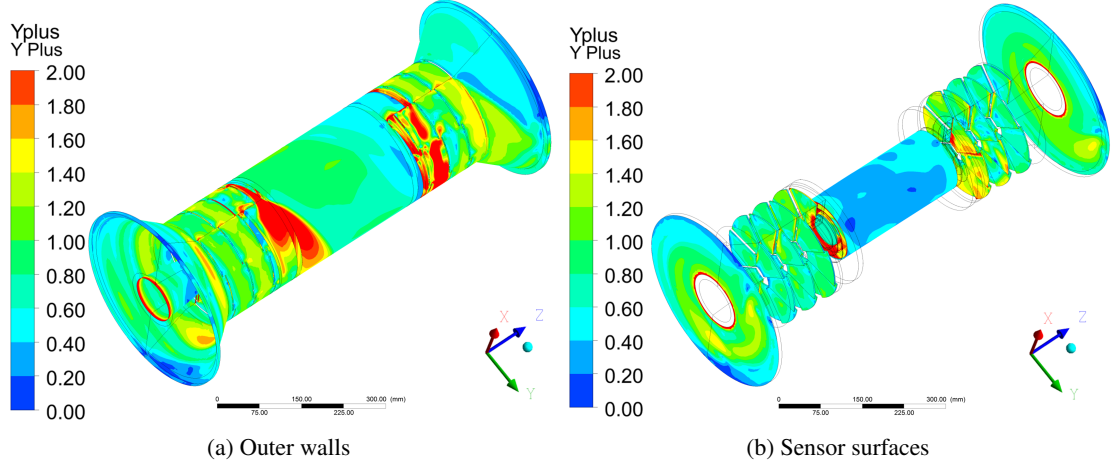


Figure 13: y^+ distribution over the solid surfaces of the vertex detector CFD model.

Plots of the velocity streamlines are shown in Figure 14. The results indicate that the tangential component of the velocity that was introduced inside the conical supply duct is sufficient to allow the air to flow across the vertex detector volume with minimal losses. The analysis of the streamline plots reveals that the air flows over the sensor surfaces in an uniform way across the volume, including in the downstream endcap region. This is mostly due to the design of the barrel support structure which minimizes the amount of disturbances in the transition from the endcap to the barrel region (as shown in detail in Figure 14c). The flow also exhibits a good (but not optimal) uniformity inside the barrel region, where the average velocity at the x-y plane is 6.3 m/s. Nevertheless, since this model includes a simplified design of the barrel layers, the real value of the average velocity inside the barrel is expected to be below the calculated one (see §2.3). One can also observe that the average velocity between the outermost barrel layer and CFRP support tube is comparatively low (2.2 m/s). This result is due to the large cross-section of this region when compared with the cross-section of the volumes in-between the inner layers of the barrel. As it will be shown later, this would result in higher surface temperatures of the outermost barrel layer. The average velocity at the outlet is 6.7 m/s.

The pressure drop from the inlet to the outlet is 463 Pa⁵). This means that the outlet pressure of 0 Pa specified in the supply duct simulation does not correspond to the reality. Nevertheless, since the properties of the air are not expected to change significantly over the pressure range mentioned, the chosen approach for the modelling of the different volumes is still considered to be valid.

⁵This is however only an indicative value due to the simplifications introduced in the model (smooth walls, flat sensitive layers, no cables, etc.). The real value of the pressure drop inside this volume is expected to be higher.

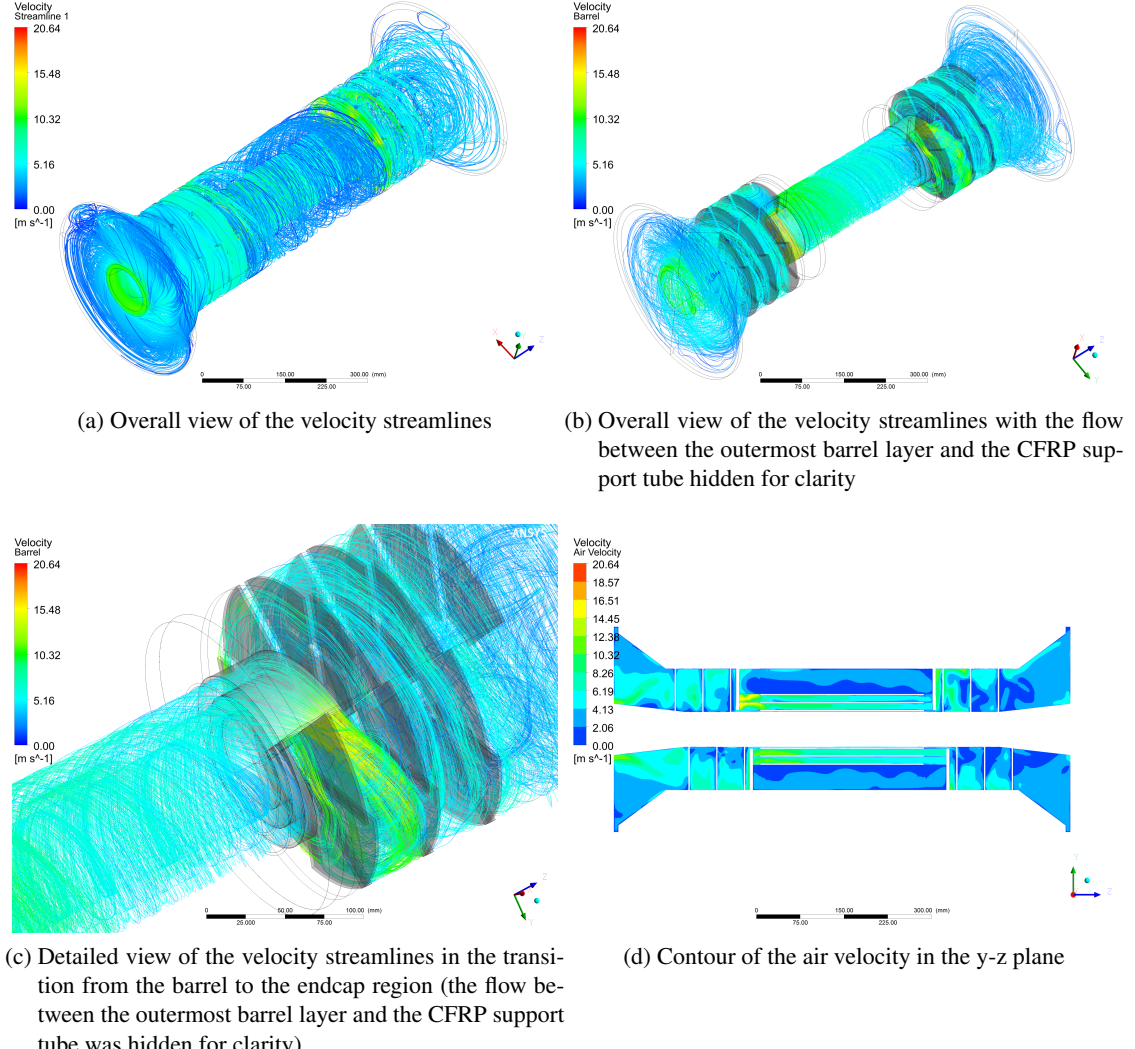


Figure 14: Air velocity inside the vertex detector volume.

The air temperature on a cross-section along the y-z plane is shown in Figure 15. As expected, the air temperature increases gradually as the flow progresses through the vertex detector volume. For an inlet temperature of 0°C the average air temperature at the outlet is 23.4°C . If an energy balance is applied to the volume:

$$q_{in} = q_{out} = m \cdot c_p (T_{out} - T_{in}) \quad (3)$$

it yields that, for a mass flow m of 19.9 g/s , a specific heat capacity at constant pressure c_p of 1004.4 J/kgK and a temperature difference of 23.4°C , the calculated heat flow absorbed by the air is $q_{out} = 468.2 \text{ W}$. The heat flow applied through the boundary conditions is $q_{in} = 455.1 \text{ W}$ which differs 2.9% with respect to the calculated one. As expected due to the relatively

low air velocity, there is a heat build-up near the surface of the outermost barrel layer, with the calculated maximum value being 107.4° C.

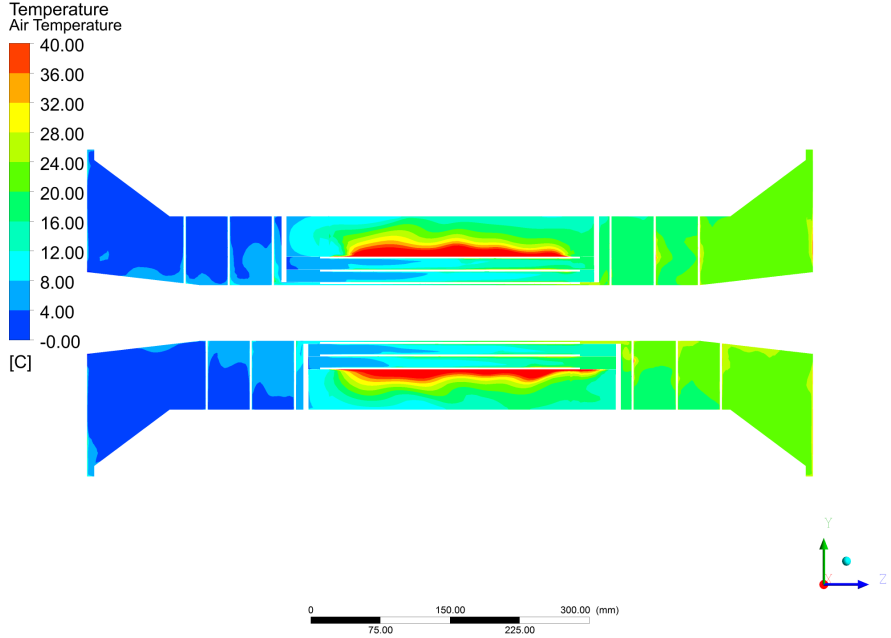


Figure 15: Air temperature inside the vertex detector volume in the y-z plane (for clarity purposes, the maximum value in the plot was capped at 40° C).

In what concerns the sensor surface temperatures, their average values⁶⁾ are presented in Table 3 and their distribution is shown in Figure 16. In the vertex detector, with the exception of the outermost barrel layer, the air flow is able to maintain average surface temperatures below 30° C. In order to reduce the surface temperature of the outermost barrel layer, it is proposed that an additional CFRP shell be added surrounding the outermost layer (as shown in Figure 17), as a means to increase the air velocity in the vicinity of the sensor surface. The impact of this geometry modification needs to be evaluated in future simulations of the vertex detector volume. The analysis of Figure 16 indicates that the temperature distribution along the sensor surfaces is not homogeneous, with high and low temperature areas appearing very close to each other. This is due to the fact that the model does not account for the in-plane heat transfer through conduction inside sensors/readout chips and their support structure. One can therefore expect that the addition of this phenomenon to the model will result in higher temperature homogeneity along the

⁶⁾The maximum temperature values are not shown since they are not meaningful if conductive heat transfer is not included in the model. For a convective only heat transfer simulation, the surface temperature is calculated on the basis of the Newton's law of cooling $T_s = \frac{q}{h} + T_\infty$, where the surface temperature T_s is a function of the convective heat flux q , the convective heat transfer coefficient h and the temperature of the fluid T_∞ . If locally there is a low convective heat transfer coefficient (due for instance to a low fluid velocity), the result would be a peak in the surface temperature. In reality, if such flow conditions occur, the heat transfer through conduction within the surface and between the surface and the fluid will take over and attenuate these temperature peaks.

sensor surfaces (an example of this effect can be seen in §2.3). In addition, it can be seen from the analysis of Figures 16a, b and c, that there is a considerable temperature difference between adjacent surfaces that form a single module (double-sided ladders and petals). This difference is due to the fact that the out-of-plane heat transfer through conduction in the modules was also not included in the model. In reality, due to the small thickness of these modules (approximately 2 mm), it is expected that the temperature difference between the two sides of the module be much smaller. Furthermore, heat transfer through radiation is also not included in the model, which, once accounted for, is expected to marginally improve the temperature homogeneity.

The model presented in this chapter is therefore not expected to yield precise temperature distributions but instead to provide a qualitative view of the performance of the cooling strategy proposed in this note. Detailed analyses will require a more mature design of the inner region, with more information regarding sensor and readout technologies, power consumption distribution, support structure materials, etc. as well as a validation through experimental measurements on a prototype test bench.

Table 3: Average temperatures at the surface of the sensors.

Location	Average temperature (in $^{\circ}$ C)
VTX barrel layer #1	23.6
VTX barrel layer #2	22.8
VTX barrel layer #3	19.4
VTX barrel layer #4	26.5
VTX barrel layer #5	21.1
VTX barrel layer #6	79.5
VTX petals (negative z-coordinate)	12.0
VTX petals (positive z-coordinate)	27.1
FTD #1 (negative z-coordinate)	12.6
FTD #1 (positive z-coordinate)	32.5

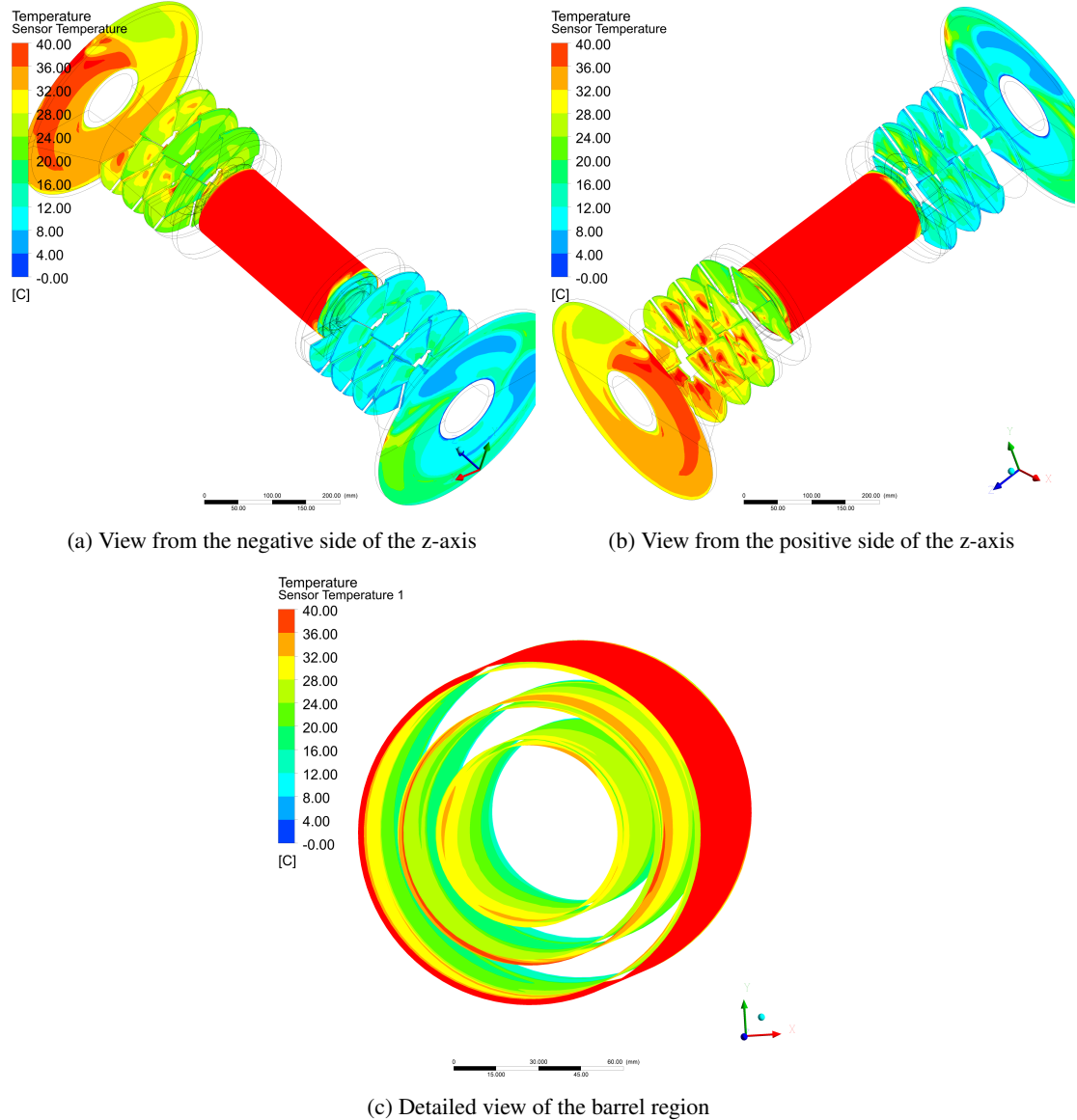


Figure 16: Sensor surface temperature (for clarity purposes, the maximum value in the plot was capped at 40° C).

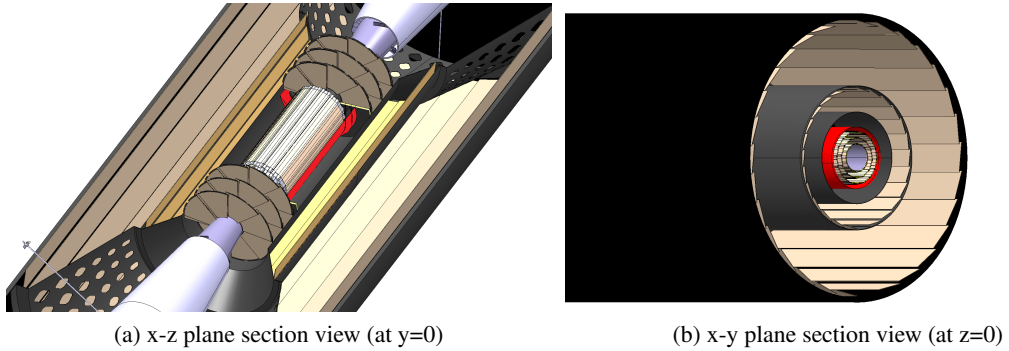


Figure 17: Proposal for a CFRP shell (shown in red) to surround the outermost vertex barrel layer.

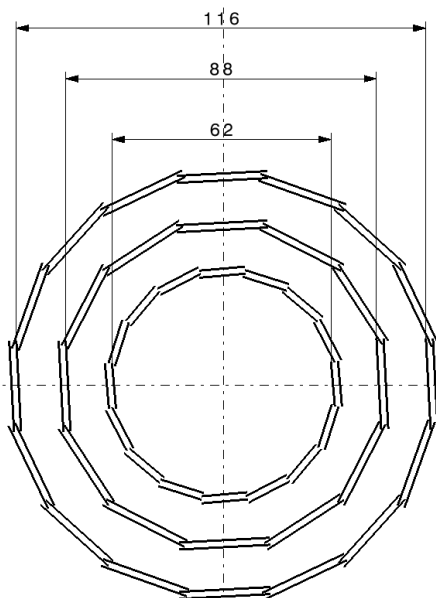


Figure 18: Possible ladder layout inside the vertex detector barrel. 16 double-sided ladders are equally distributed along the circumferential direction in the inner and outermost layers, whilst the middle layer is composed of 12 double-sided ladders. Shown are the inner diameters of each layer (in millimeters).

2.3. Vertex Detector Barrel Submodel

As mentioned in the previous chapter, the model created for the analysis of the vertex detector volume included a simplified representation of the barrel region. Although enough to simulate the overall flow inside the vertex detector volume, this simplification did not allow an accurate evaluation of the flow characteristics between the barrel ladders. As a consequence, three de-

tailed models have been created to simulate the flow conditions between the beam pipe and the innermost barrel layer, layers number 2 and 3 and layers number 4 and 5. The geometries used in these models present a polygonal cross-sectional shape intended to represent the ladder layout shown in Figure 18. Their cross-section is shown in Figure 19. In order to account for the heat transfer by conduction inside the ladder, a set of stacked solid volumes was introduced in the model following the possible double-sided ladder layup shown in Figure 20. Since the design for ladder support structure is not yet known, only the sensor, readout, glue and cable were modelled. As such, the heat transfer by conduction from one side of the ladder support structure to the other was not modelled. Furthermore, in order to simplify the simulation, only one layup per barrel layer was introduced.

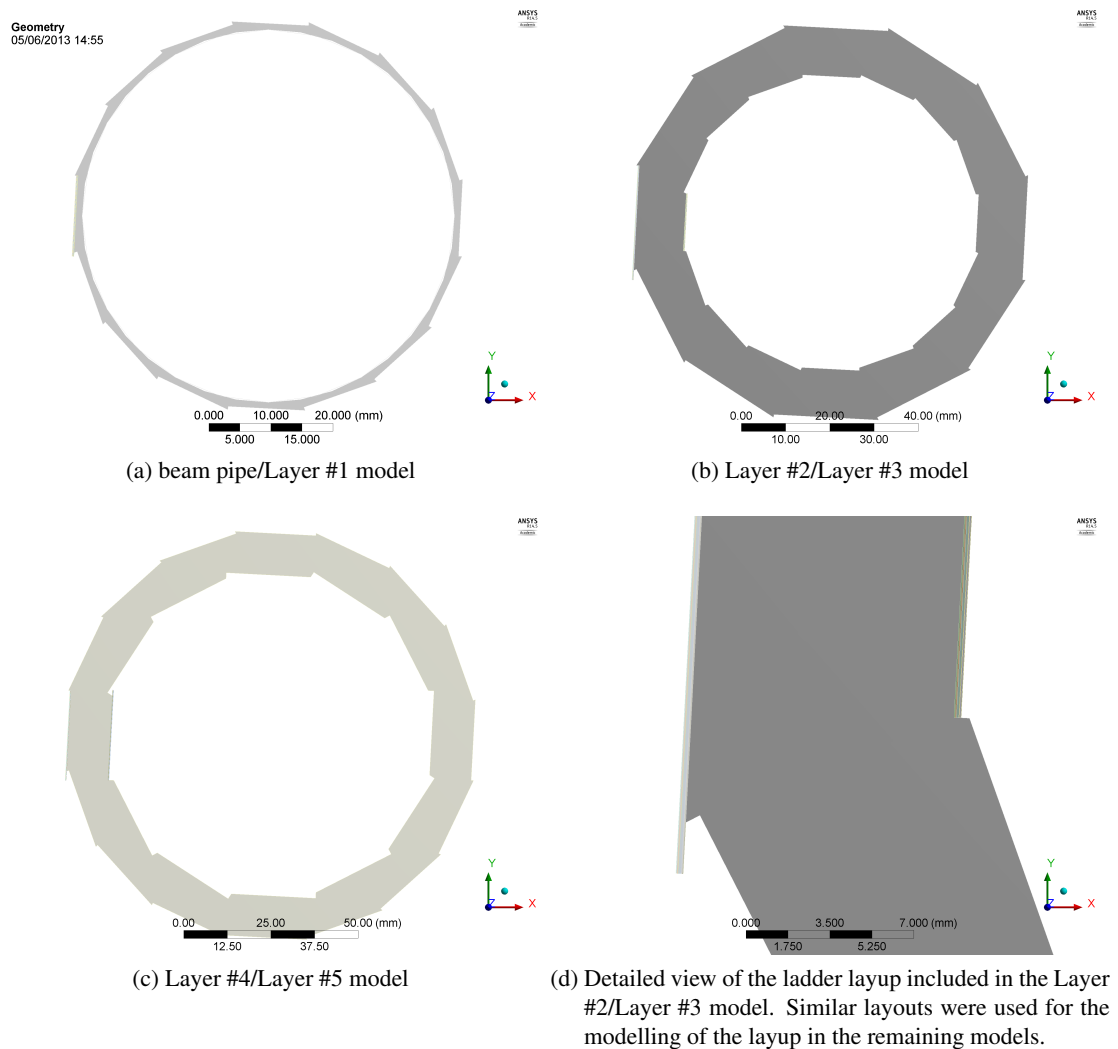


Figure 19: Cross-sectional view of the geometries used in the detailed modelling of the vertex detector barrel volume.

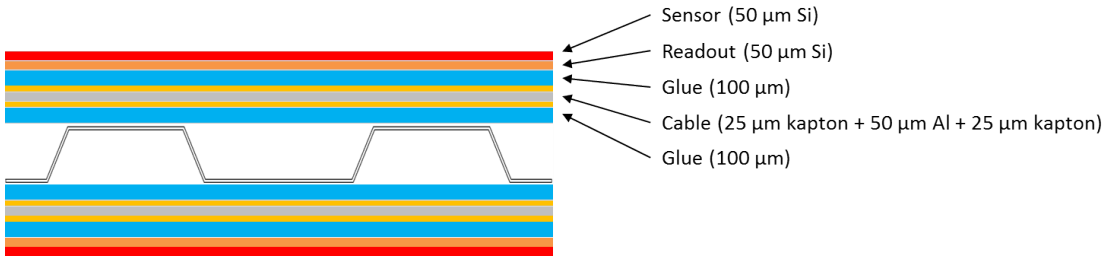


Figure 20: Sketch showing the different layers of a possible double-sided ladder.

The meshes that were generated in the geometries presented above are shown in Figure 21 and have the characteristics shown in Table 4. For the modelling of the solid layers, a typical element size of 1 mm was used, with a minimum of three elements through the thickness.

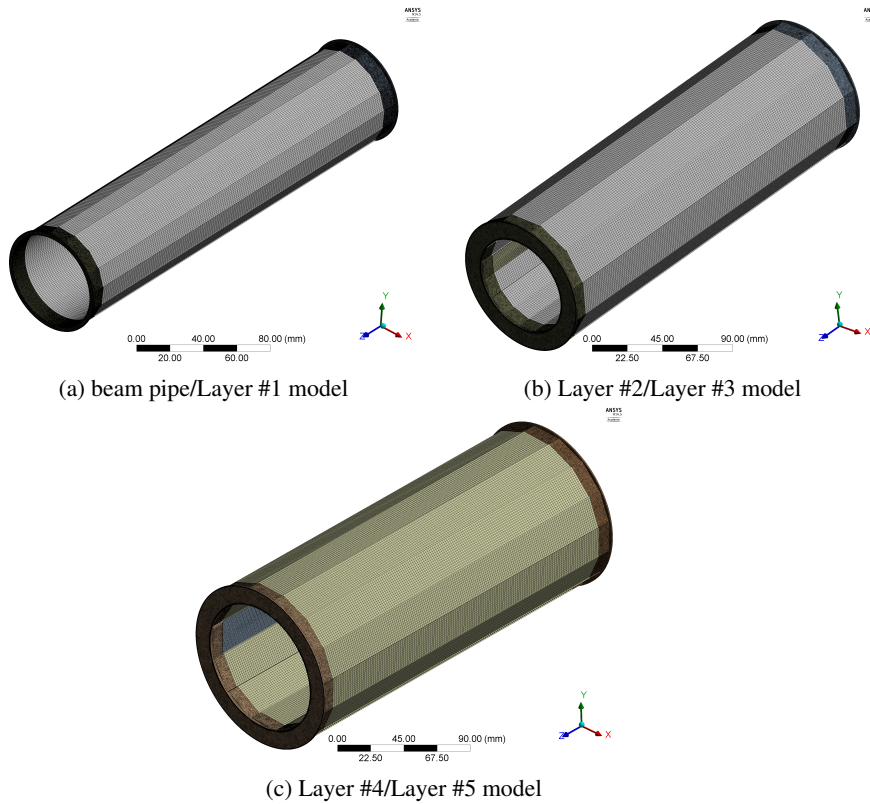


Figure 21: Meshes for the different detailed models of the vertex detector barrel region.

Table 4: Characteristics of the vertex detector barrel model mesh.

Model	Element size in sensor region	Element size in inlet/outlet regions	Cell count
beam pipe/Layer #1	1.0 mm	0.4 mm	3.8×10^6
Layer #2/Layer #3	1.3 mm	0.7 mm	3.8×10^6
Layer #4/Layer #5	1.5 mm	0.9 mm	3.1×10^6

In order to account for the flow upstream and downstream from the barrel, the velocity and temperature distributions on the plane $z = -141$ mm and the pressure and temperature distributions on the plane $z = 141$ mm obtained from the results of the model presented in §2.2 were used to specify the inlet and outlet conditions in the detailed barrel models respectively. An overview of the remaining boundary conditions is shown in Figure 22.

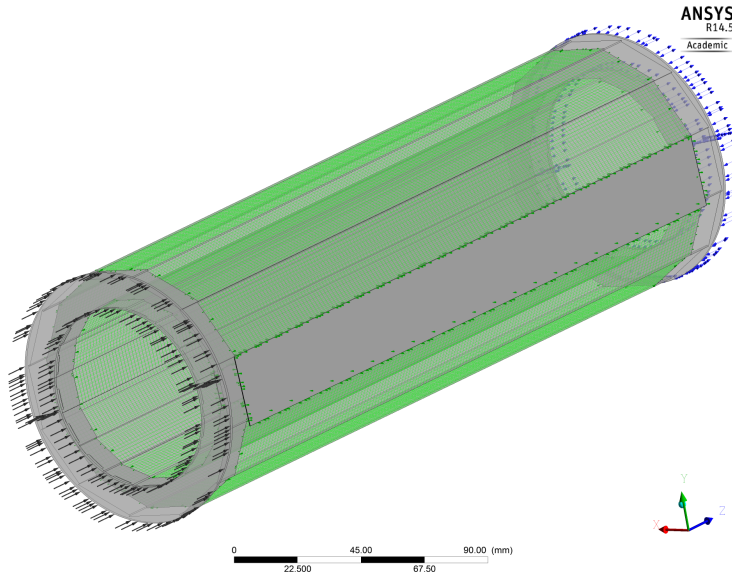


Figure 22: Overview of the boundary conditions applied to the Layer #2/Layer #3 detailed barrel model. In green are shown the surfaces where a 50 mW/cm^2 heat flux was applied. Where the solid layup was introduced (gray rectangular surface), the heat flux was applied by means of a $1 \times 10^7 \text{ W/m}^3$ volumetric source in the readout solid volume (this yielded an equivalent surface heat flux of 50 mW/cm^2). All other surfaces were considered to be adiabatic. The inlet and outlet are identified by the black and blue arrows respectively. Similar boundary conditions were applied to the two other detailed barrel models.

The air was modelled using the "Air at 25° C " material properties available in the ANSYS CFX library with a reference pressure of 1 atm being specified. The properties of the solid materials as presented in Table 5.

The simulation of the heat transfer inside the air was done using the "Thermal Energy" heat transfer option, with the turbulence being modelled through the use of a $k-\omega$ SST model. The analysis was defined as steady-state with an auto timescale as well as an RMS residual target of 10^{-4} and a conservation target of 10^{-2} as convergence criteria. The solution was allowed to run from a minimum of 200 to a maximum of 400 iterations. The corresponding convergence plots are shown in Figures 23, 24 and 25.

Table 5: Physical properties of the solid materials included in the detailed vertex detector barrel simulations.

Component	Material	Density [kg/m ³]	Specific Heat Capacity [J/kgK]	Thermal Conductivity [W/mK]
Sensor	Silicon	2330	710	148
Readout	Silicon	2330	710	148
Glue	AralditeB	1200	1050	0.2
Cable	Kapton	1420	1090	0.12
	Aluminium	2700	903	237

The y^+ distribution over the solid surfaces of the models is shown in Figure 26. The results show that the overall values of the y^+ variable are within the recommended range and therefore confirm the ability of the mesh/turbulence model to describe the near wall behaviour of the flow. The average Reynolds numbers in the different models range from 1.3×10^4 to 2.6×10^4 , which also confirms the assumption of a turbulent flow regime.

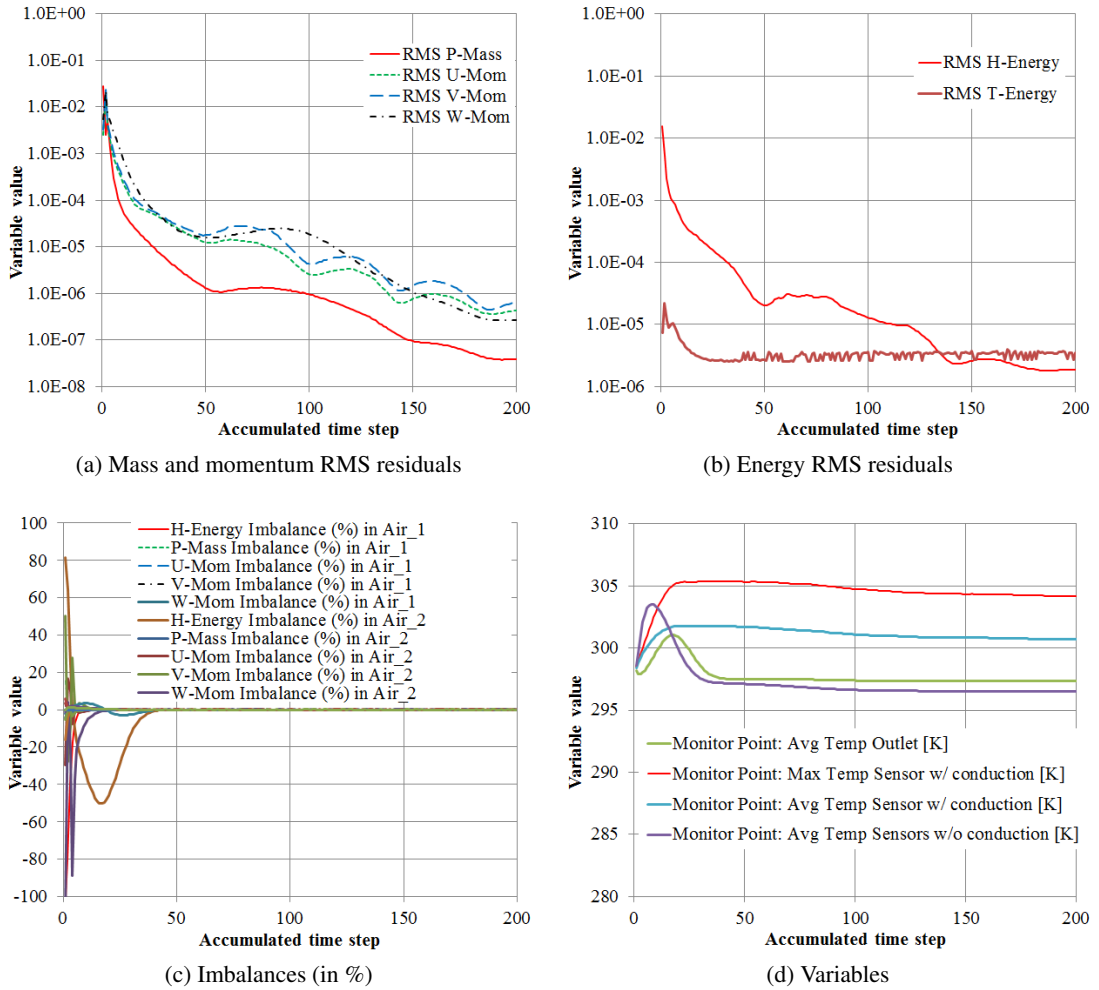


Figure 23: Convergence plots of the beam pipe/Layer #1 model solution process. Both the RMS residuals and imbalances achieved the convergence targets.

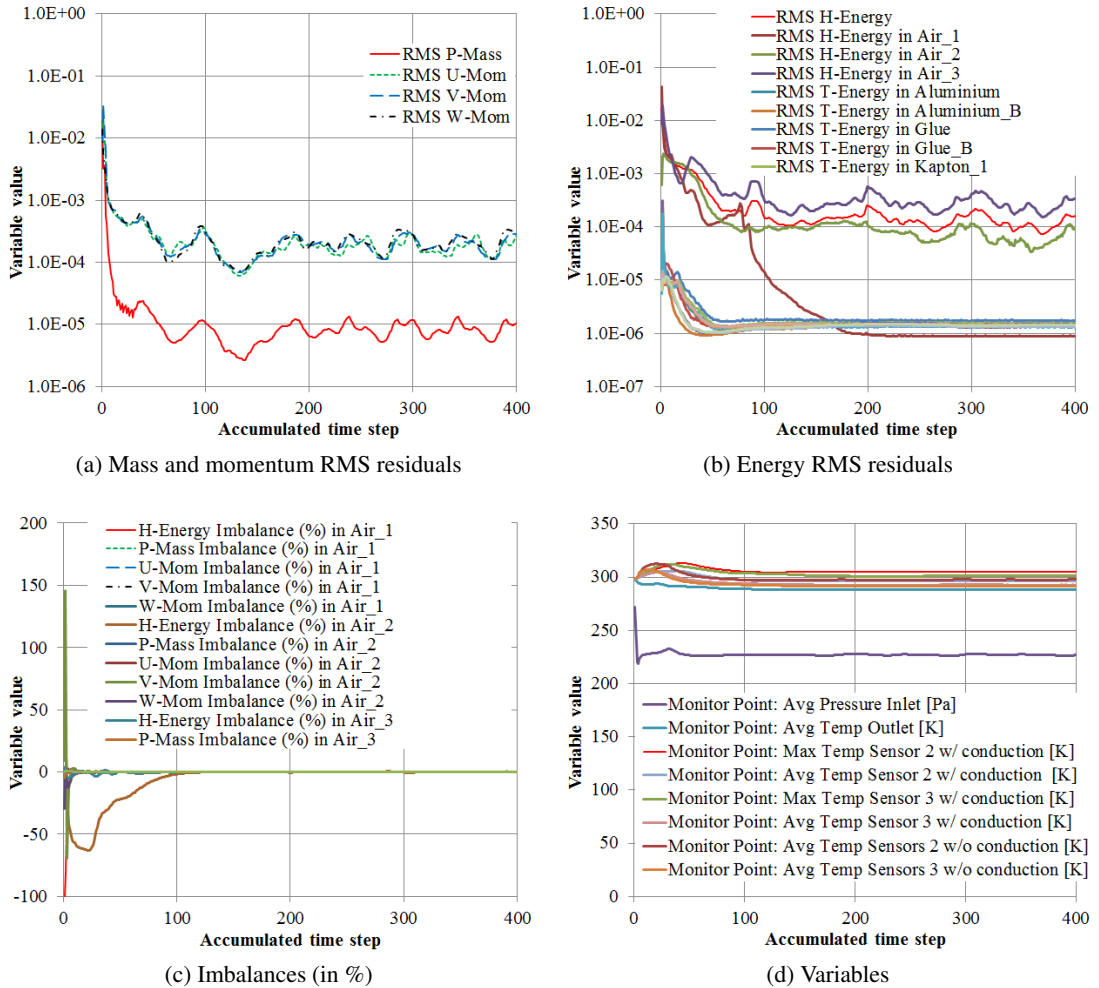


Figure 24: Convergence plots of the Layer #2/Layer #3 model solution process. The RMS residuals and imbalances did not achieve the convergence targets; however, the values of the variables of interest achieved steady-state conditions.

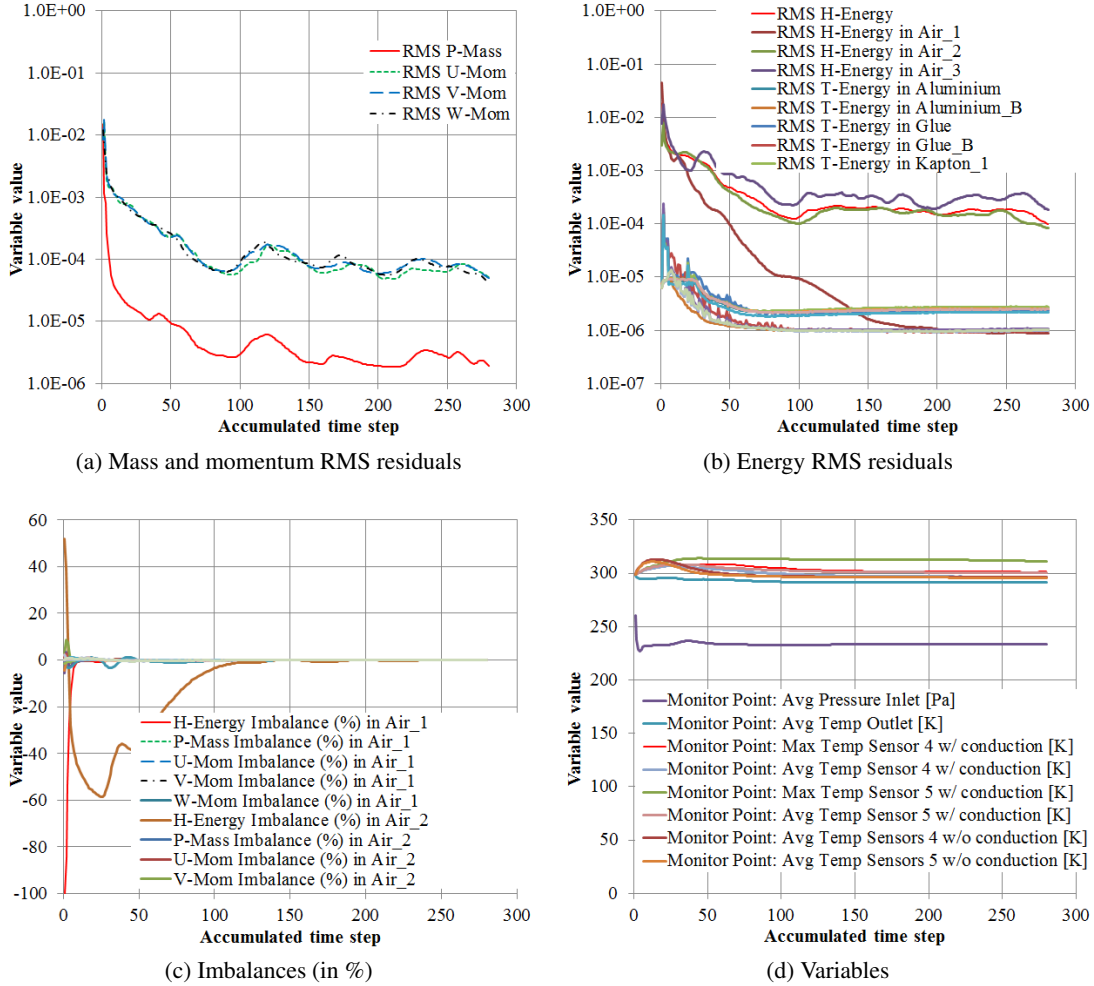


Figure 25: Convergence plots of the Layer #4/Layer #5 model solution process. Both the RMS residuals and imbalances achieved the convergence targets.

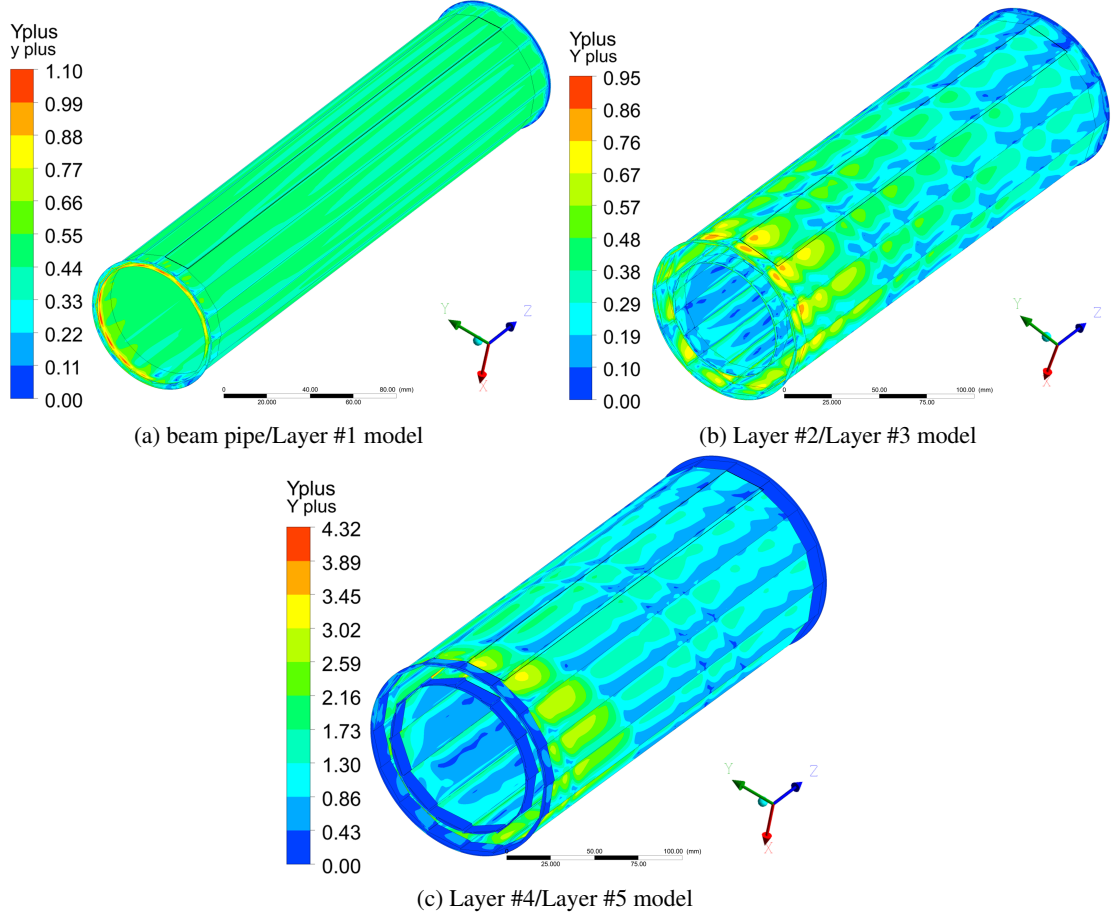
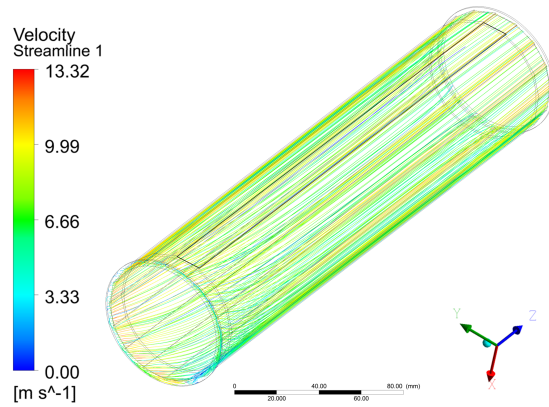
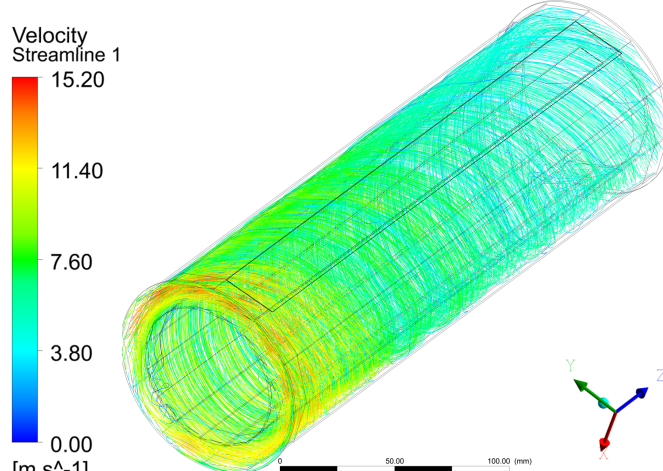


Figure 26: y^+ distribution over the solid surfaces of the vertex detector barrel detailed models.

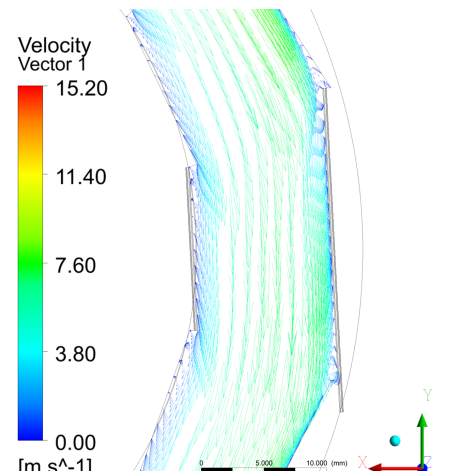
The air velocity distribution inside the volumes of each barrel model is shown in Figure 27. The results indicate that the velocity streamlines between the beam pipe and the innermost barrel layer are mainly longitudinal. This is due to the fact that the innermost layer is placed very close to the beam pipe with, as a consequence, the rotational momentum of the flow being lost due to the increased losses. In what concerns the flow between barrel layers #2/#3 and #4/#5, the rotational momentum of the flow is preserved throughout the barrel, despite the more complex layout. In the x-y plane at $z=0$, the average velocity in the multiple volumes is 6.3 m/s, 5.3 m/s and 3.7 m/s from the innermost to the outermost volume respectively. The fact that the average velocities differ significantly from one volume to the other indicates that further optimization studies of the geometry of the barrel support structure are needed.



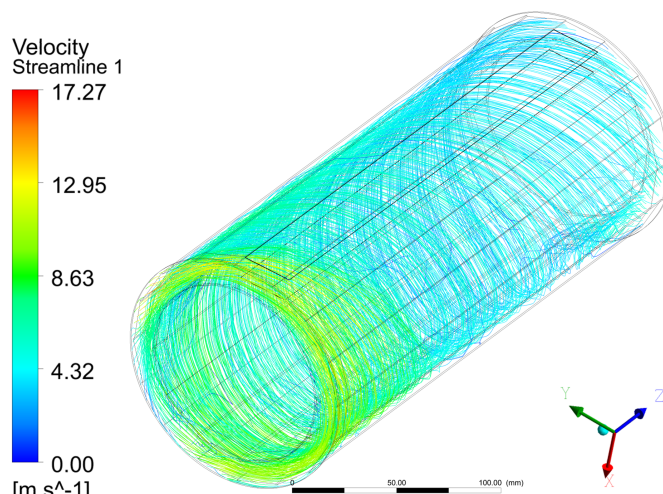
(a) beam pipe/Layer #1 model streamlines



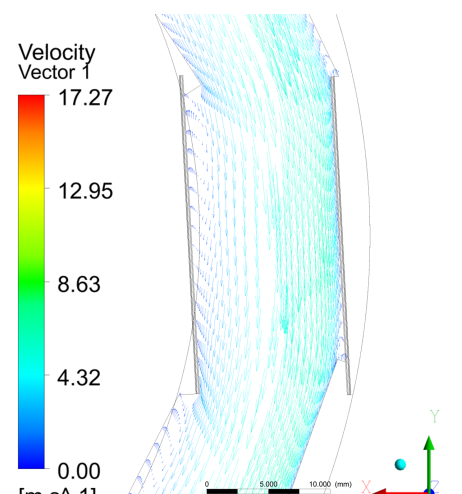
(b) Layer #2/Layer #3 model streamlines



(c) Layer #2/Layer #3 model vector plot in the x-y plane (at z=0)



(d) Layer #4/Layer #5 model streamlines



(e) Layer #4/Layer #5 model vector plot in the x-y plane (at z=0)

Figure 27: Air velocity in the vertex detector detailed models.

When compared with Figure 16c, the more detailed modelling of the vertex detector barrel yielded a different temperature distribution on the sensor surfaces. Furthermore, the modelling of heat transfer by conduction in some ladders of the barrel resulted in more a uniform temperature distribution on the sensor surface with a reduction of the peak temperature values (see Figures 28 and 29). A profile of the surface temperatures along the ladder length is shown in Figure 29f. The analysis of Figure 29f shows that there is an important temperature difference between the extremities of each layer (between 10° C and 23.5° C depending on the layer) which is common in air cooled designs. Nevertheless, an optimization of the barrel support structure would allow to improve these values. Another result of the analysis of Figure 29f is that there exists a considerable difference of temperatures between the layers that would form a double-sided ladder. Although this is in part a result of a non-optimized flow, the model did not account for heat transfer by conduction between adjacent layers which, if simulated, would significantly reduce this temperature difference. With exception of barrel layer #5, the ladder temperature is kept below 30° C.

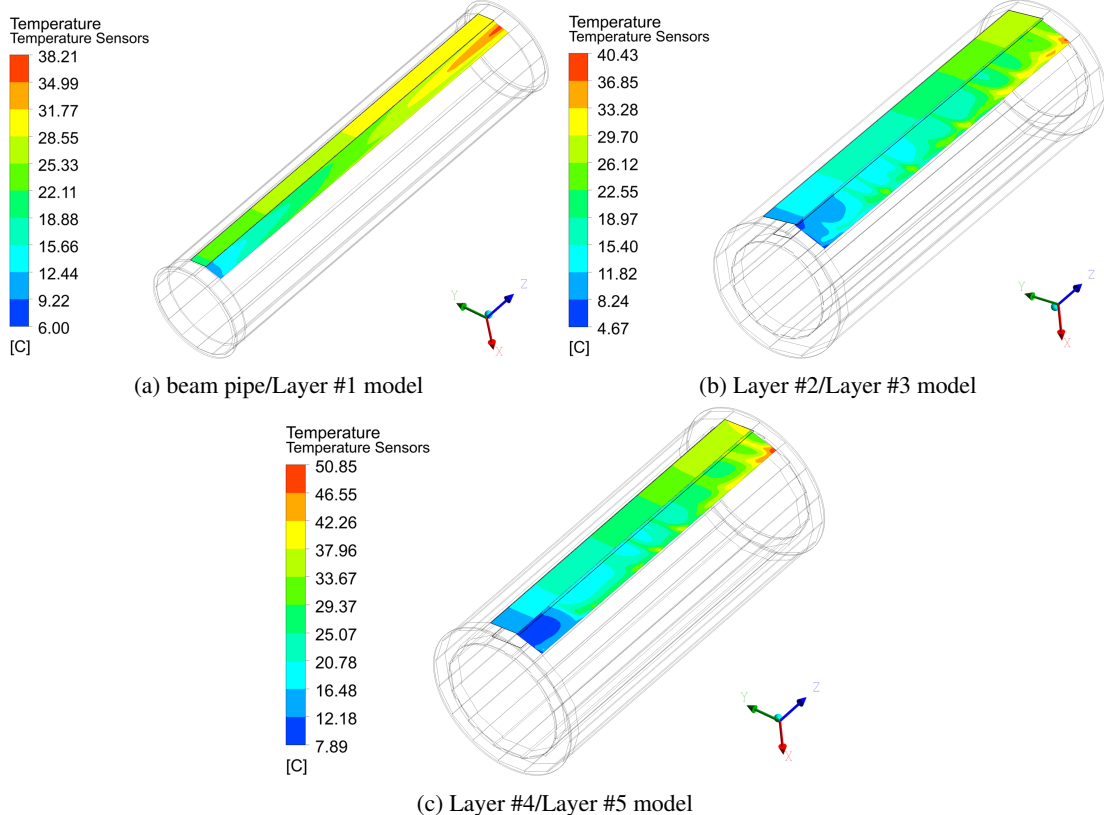


Figure 28: Temperature distribution over the sensor surfaces of the vertex detector barrel detailed models (in each picture, the ladder on the left includes conduction whilst the ladder on the right does not). The distribution changes significantly from the layers with no heat transfer by conduction to the ones were it has been included in the model; as expected, with conduction, a more uniform temperature distribution is achieved with the peak values being comparatively lower.

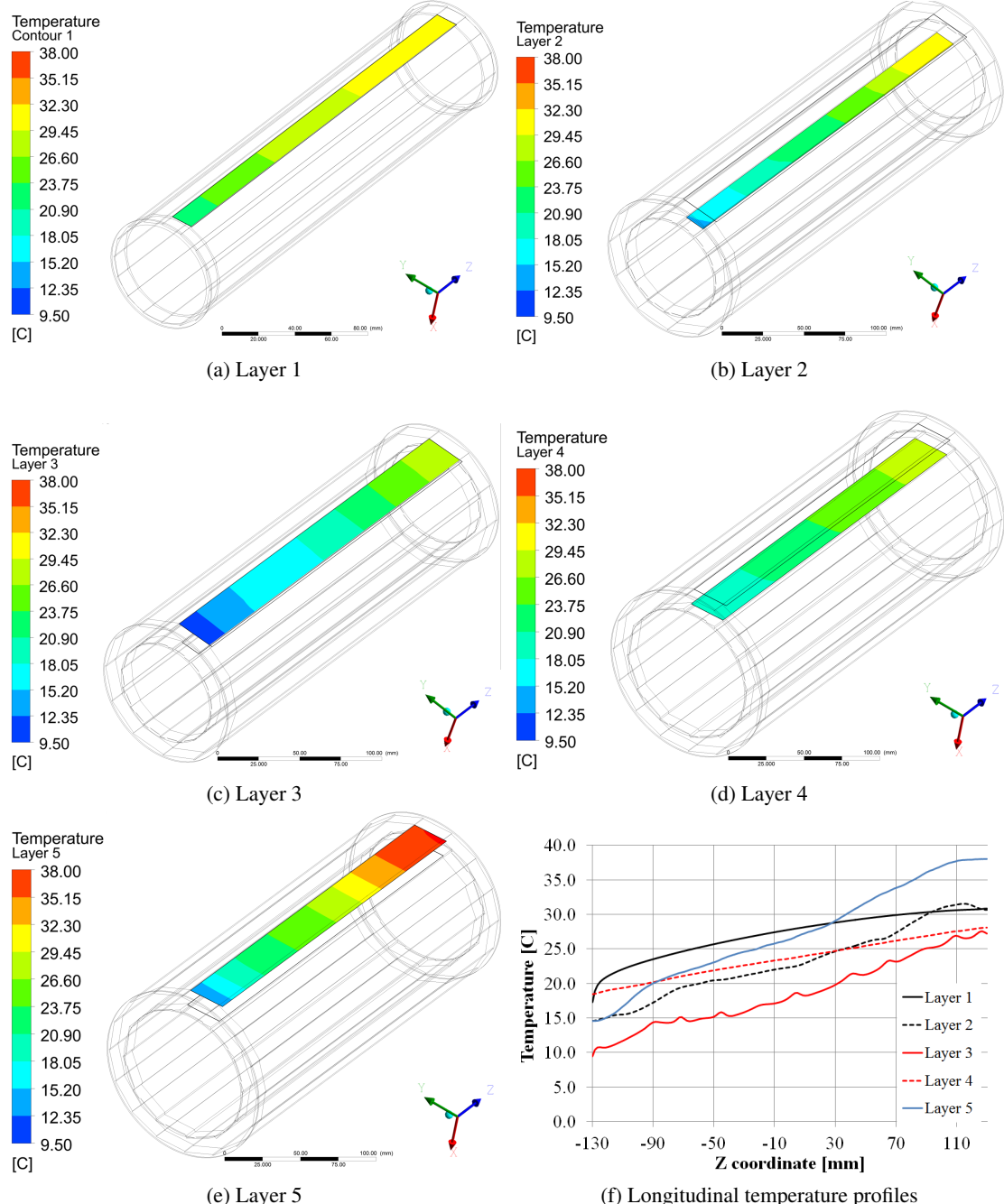


Figure 29: Temperature distribution along the different layers (where heat transfer by conduction was included) in the vertex detector detailed models.

2.4. Single Ladder Simulations

In order to simulate the cooling of a single double-sided ladder, including heat transfer through convection and conduction, two 2D models of a ladder in a transverse and longitudinal flows respectively were created (the geometry and boundary conditions are illustrated in Figures 30a and 30b). In the Figures, the air inlet ($v = 4 \text{ m/s}$ and $T = 0^\circ \text{ C}$) is on the left of the domain and the outlet ($P_{rel} = 0 \text{ Pa}$) on the right. The included layup of the ladder represents the one shown schematically in Figure 20. This layup is placed on each side of a generic CFRP support structure. The mesh of these models is one cell deep so that no flow in the direction normal to the domain is allowed. Steady-state analyses were performed with the convergence plots shown in Figures 31 and 32. Both analyses achieved the convergence targets specified (RMS residuals of 10^{-4} and a conservation target of 10^{-2}).

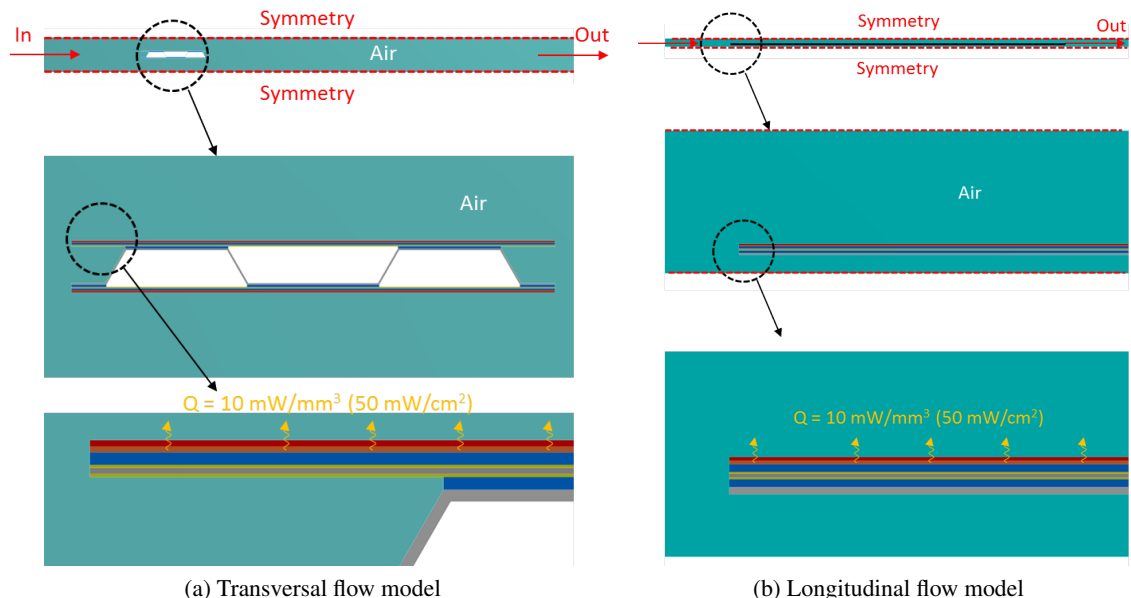


Figure 30: Geometry and boundary conditions of the 2D models used to simulate the cooling of a double-sided ladder in both a transverse and longitudinal flow (the ladder width and length are 25.85 mm and 260 mm, respectively).

The results of the simulations are shown in Figures 33, 34 and 35. In Figure 33a it is possible to observe that the non-symmetric ladder support structure generates a non-symmetric flow around the ladder which, in turn, results in a one degree temperature difference between the ladder top and bottom surfaces. For the ladder in a transverse flow, the temperature distribution is mostly uniform along its width with small variations (8 to 9° C for a 0° C bulk air temperature). However, for the case where the ladder is cooled by a longitudinal flow, the temperature gradient across its length is significant (27° C) with peak values reaching about 38° C .

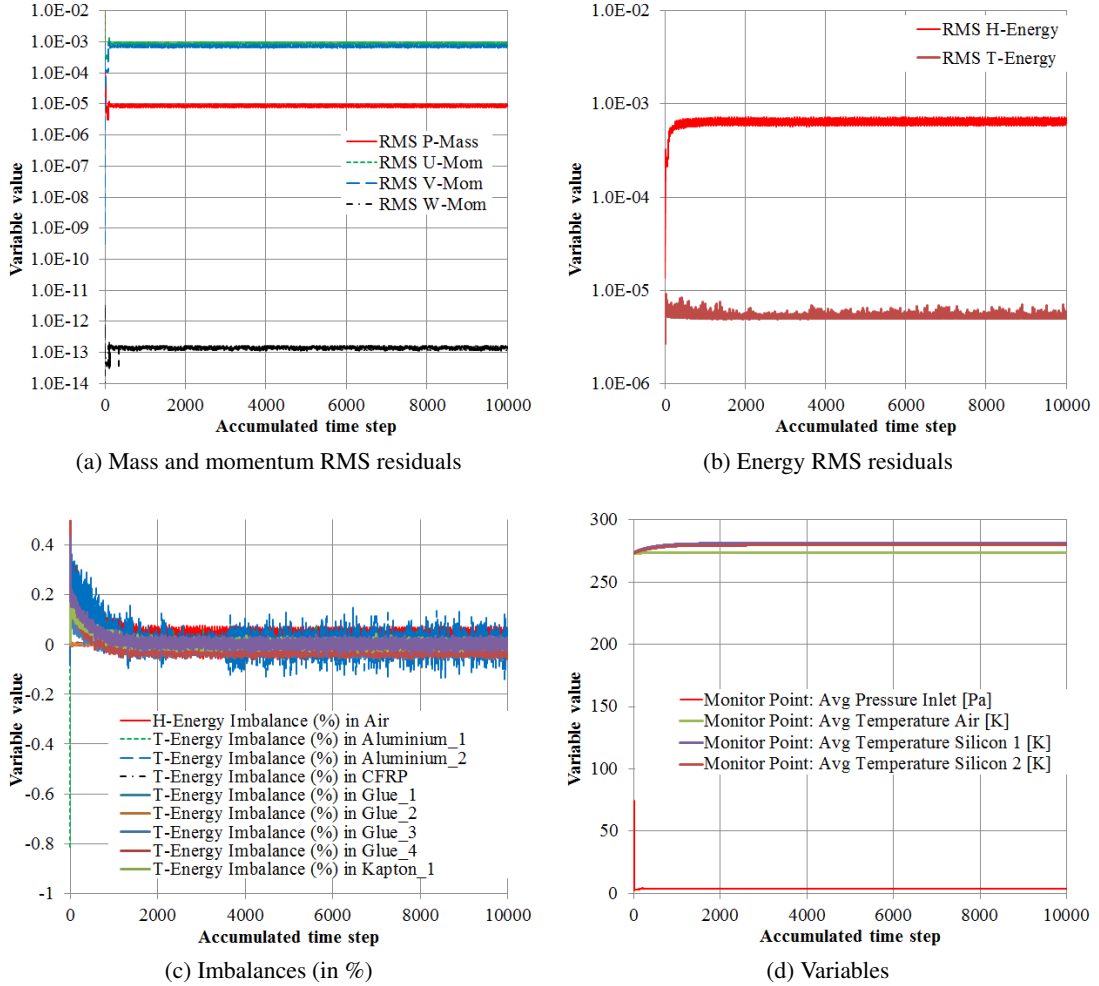


Figure 31: Convergence plots of the simulation of the cooling of a double-sided ladder in a transverse flow.

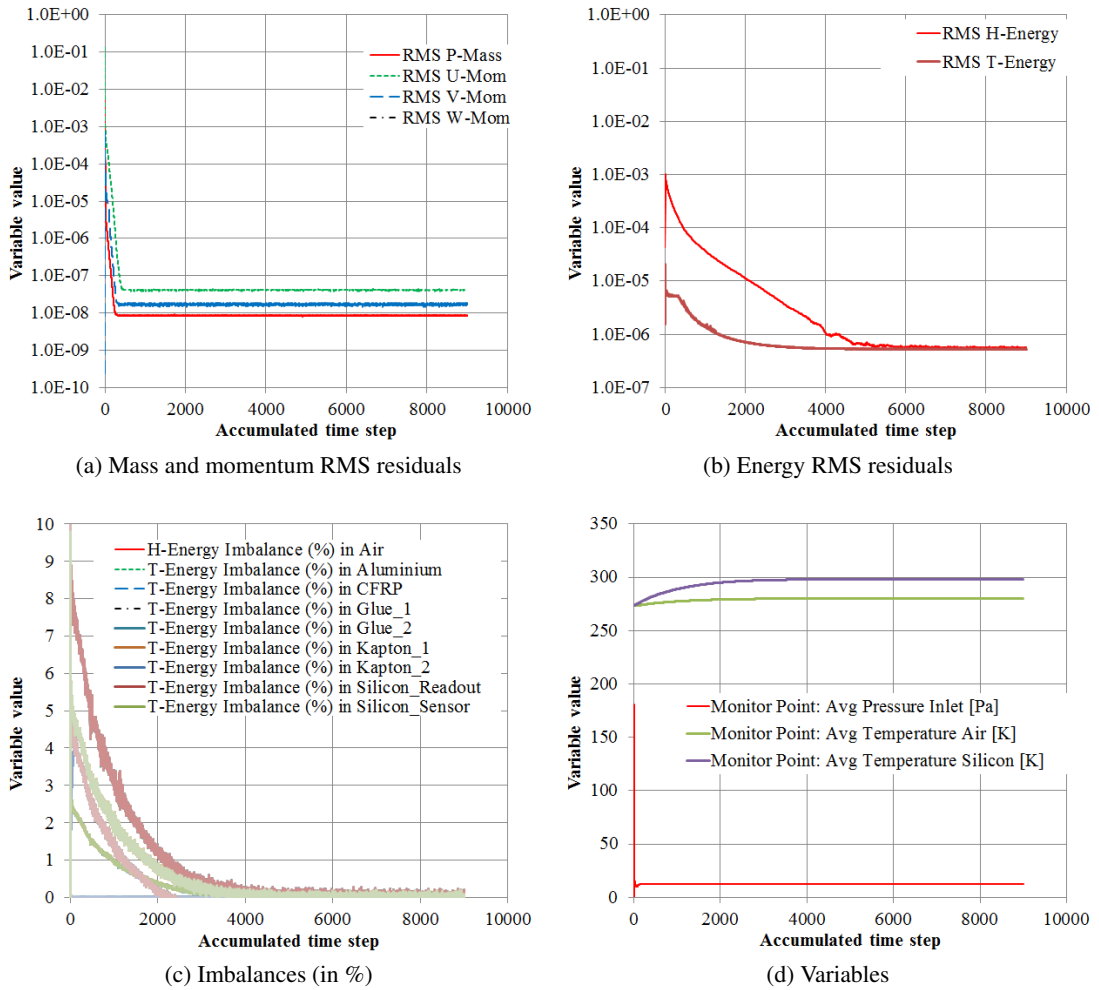


Figure 32: Convergence plots of the simulation of the cooling of a double-sided ladder in a longitudinal flow.

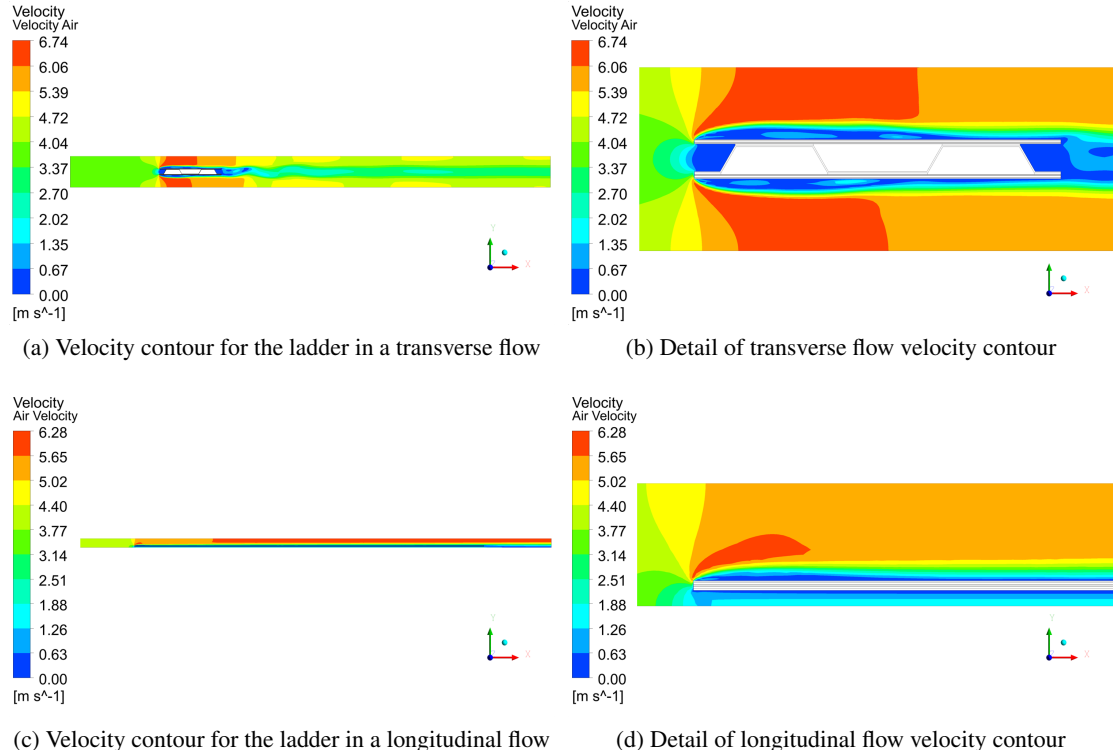


Figure 33: Velocity contour plots for the cooling of a single double-sided ladder.

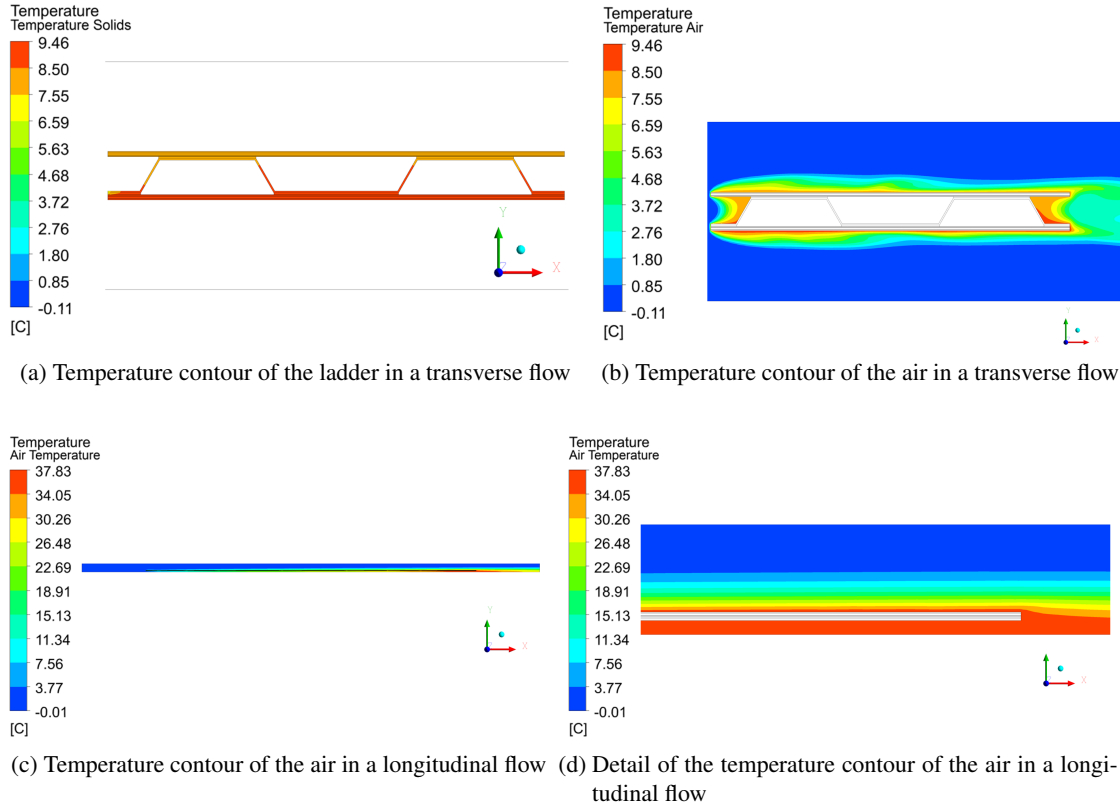


Figure 34: Temperature contour plots for the cooling of a single double-sided ladder.

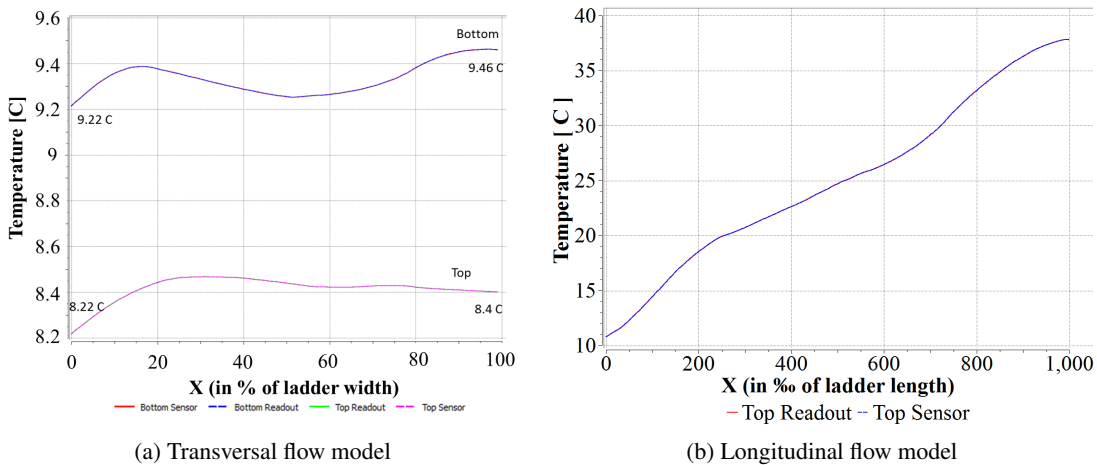


Figure 35: Temperature profile on the sensor and readout surfaces for the cooling of a single double-sided ladder.

One can therefore conclude that cooling the vertex detector barrel with a purely longitudinal flow will result, for low to moderate air velocities (below 5 m/s), in a temperature gradient which could compromise the mechanical stability of the barrel. Since it is impossible to have a purely transversal cooling stream, the helical shaped flow presented in §1.2 is intended to provide the minimum temperature gradient along the ladder length whilst at the same time being feasible from the point of view of integration.

2.5. Forward Tracking Volume

As mentioned in §1.1, the silicon tracker of the CLIC_ILD detector concept comprises five tracking disks (FTDs 1-5) that complement the tracking acceptance down to polar angles of 7° . With the exception of the innermost disk which makes use of silicon pixel technology detectors, the FTDs will use double-sided silicon micro-strip technology. This is similar to the solution proposed for the FTDs 3-7 in the ILC/ILD detector concept [7]. Since the design of the ILC/ILD FTDs is more mature than the one for the CLIC_ILD detector concept, a collaboration has been established with the design team responsible for the development ILC/ILD FTDs. The purpose of this collaboration was to evaluate the possibility of cooling the ILC/ILD FTDs by using natural convection in an air atmosphere⁷⁾. The results of this study will then also be useful for the development of the CLIC_ILD FTDs.

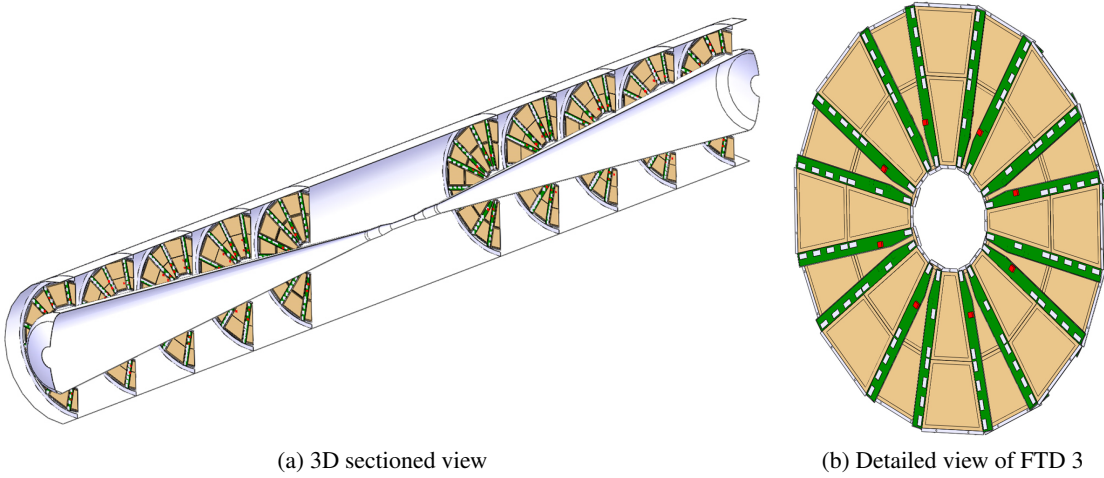


Figure 36: Geometry of the ILC/ILD FTDs 3-7 (courtesy of D. Moya - IFCA).

As described in [7], the outer FTDs of the ILC/ILD detector concept are segmented in 16 petals that are mounted in two half rings as shown in Figure 36. Each petal consists of a trapezoidal shaped frame made of CFRP while the ring is designed as a sandwich structure with two skins of high modulus carbon fibre laminate with a foam or honeycomb core. Four sensors are glued in each petal (two per petal side). The electronic hybrids will be located on the frame edge

⁷⁾To be noted that the flow conditions in this region are not related with the helical strategy proposed before.

as shown in Figure 37.

In order to simplify the analysis, whilst at the same time maximizing the amount of detail included in the model, only the cooling of a single petal was simulated (corresponding to a petal of FTD 3). In addition, the petal geometry was assumed to be symmetric with respect to both the symmetry plane of the sensors and through the petal's thickness as shown in Figure 38.

The model of the petal included heat transfer by both convection to the air and conduction within the solid volumes. The mesh used in the simulation is shown in Figure 39. It uses a combination of tetrahedral, hexahedral and prism elements, with the total cell count being approximately 2.9 millions. The typical element size in the air volume is 3 mm with the mesh in the vicinity of the solid surfaces having a typical size of 0.5 mm. In the solid volumes, the typical element size varies between 1.5 and 2 mm.

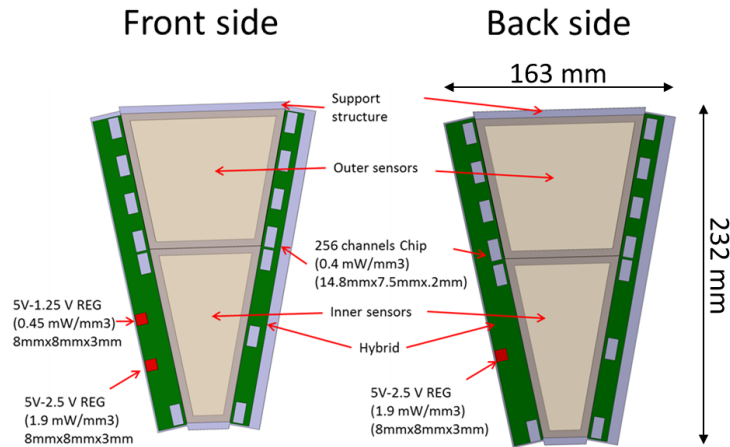


Figure 37: Engineering layout of a ILC/ILD FTD petal (courtesy of D. Moya - IFCA).
The electronic hybrids are shown in green and the voltage regulators in red.

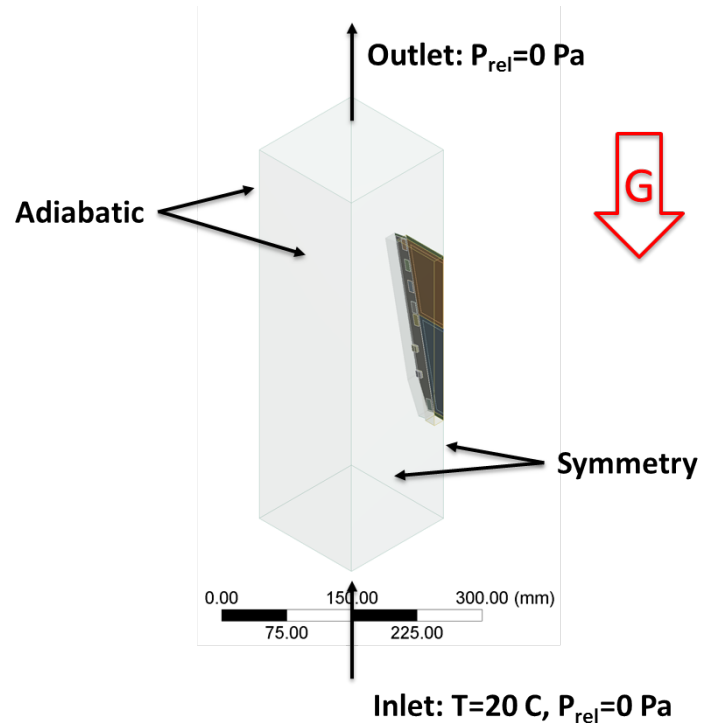


Figure 38: CFD model geometry of a quarter of a ILC/ILD FTD petal. The applied boundary conditions are also shown. A volume of air surrounds one side of the petal with the appropriate symmetry boundary conditions being applied.

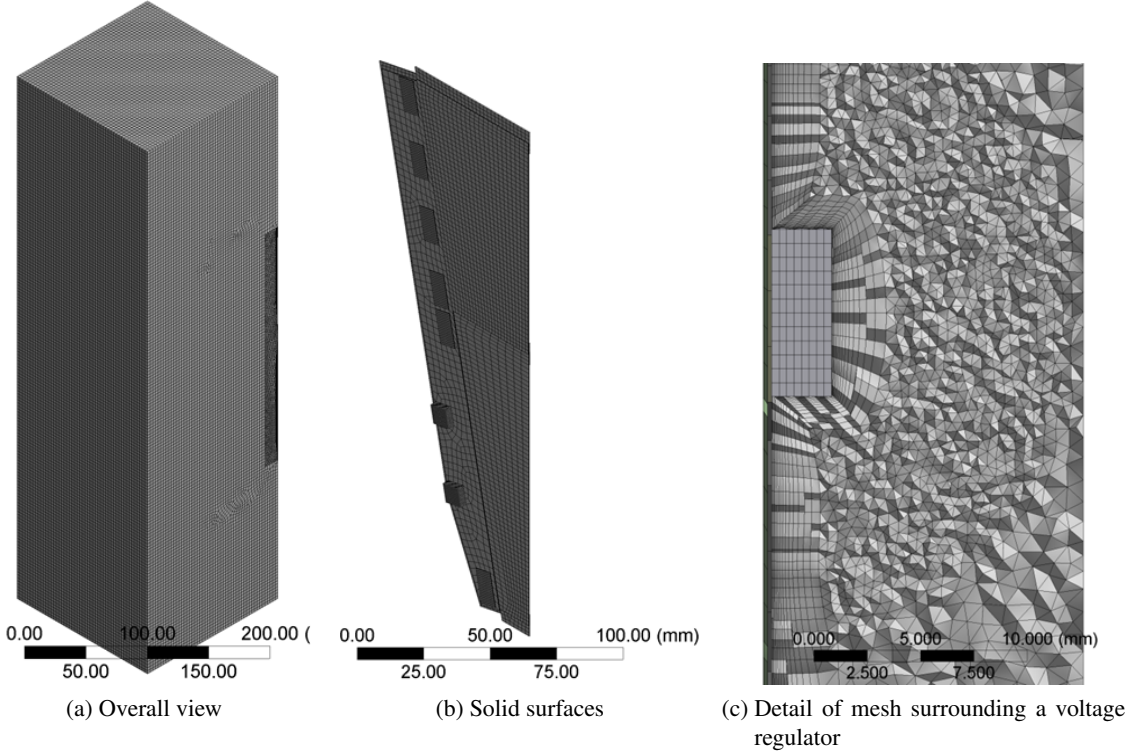


Figure 39: Mesh used for the modelling of the cooling of a ILC/ILD FTD petal.

The physical properties of the air were specified using the "Air Ideal Gas" material model of the ANSYS CFX library (a reference pressure of 1 atm was specified) with buoyancy effects being activated (i.e. natural convection) and the gravity vector applied along the direction shown in Figure 38. As for the solid volumes, the material properties used in the model are presented in Table 6. The heat transfer option "Thermal Energy" was specified and the flow was assumed to be laminar. The boundary conditions applied to the model are shown in Figure 38. In addition, volumetric heat sources were applied inside the solid volumes of the model with their magnitude and location matching the schematic drawing of Figure 37.

Table 6: Physical properties of the solid materials included in the ILC/ILD FTD petal simulations.

Component	Density [kg/m ³]	Specific Heat Capacity [J/kgK]	Thermal Conductivity [W/mK]
Sensor	2330	710	148
CFRP support	1910	711	0.96
Hybrid	1420	1090	0.12
Chips	2330	710	148
Voltage reg.	2700	896	237

The analysis was defined as steady-state with an auto timescale as well as an RMS residual target of 10^{-4} and a conservation target of 10^{-2} as convergence criteria. The solution convergence plots are shown in Figure 40. As it can be seen, the solution converged rapidly in the first hundred iterations. However, after this initial stage, instabilities have arose in the solution that lead to a stagnation of the solving process. In order to stabilize the process, the steady-state solution was interrupted after 1700 iterations and a transient process was started using as initial conditions the results from the steady-state solution. This transient analysis was allowed to run for 600 iterations until the residuals, the imbalances and the variables had achieved the initial convergence targets. The process was then concluded with a final steady-state analysis using the results from the transient solution as initial conditions.

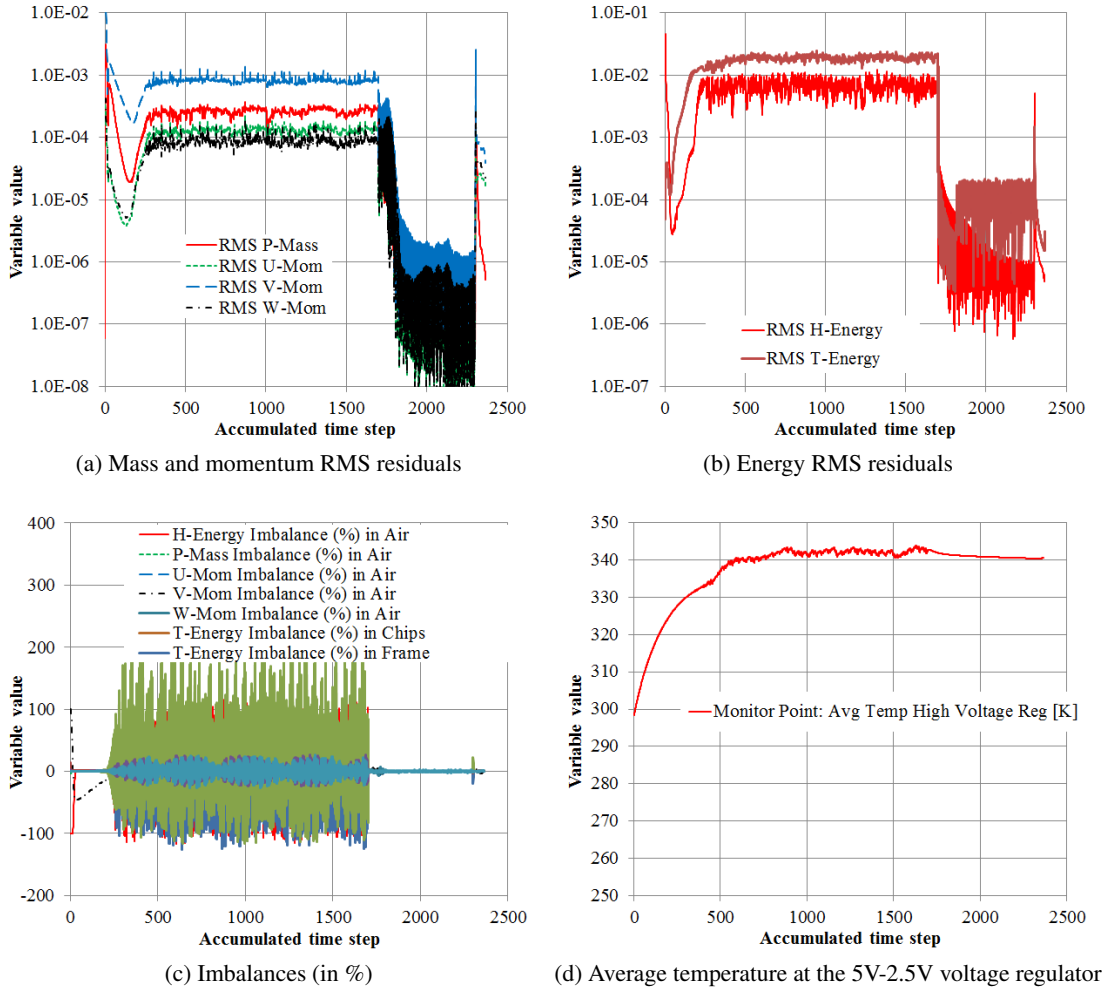


Figure 40: Convergence plots of the ILC/ILD FTD petal solution process.

The air velocity plots presented in Figure 41 show the buoyancy driven ascending currents that are created due to the heat released in the different petal components. As shown in Figure 41b,

the fine mesh near the solid surfaces is able to capture the change in flow direction near these elements.

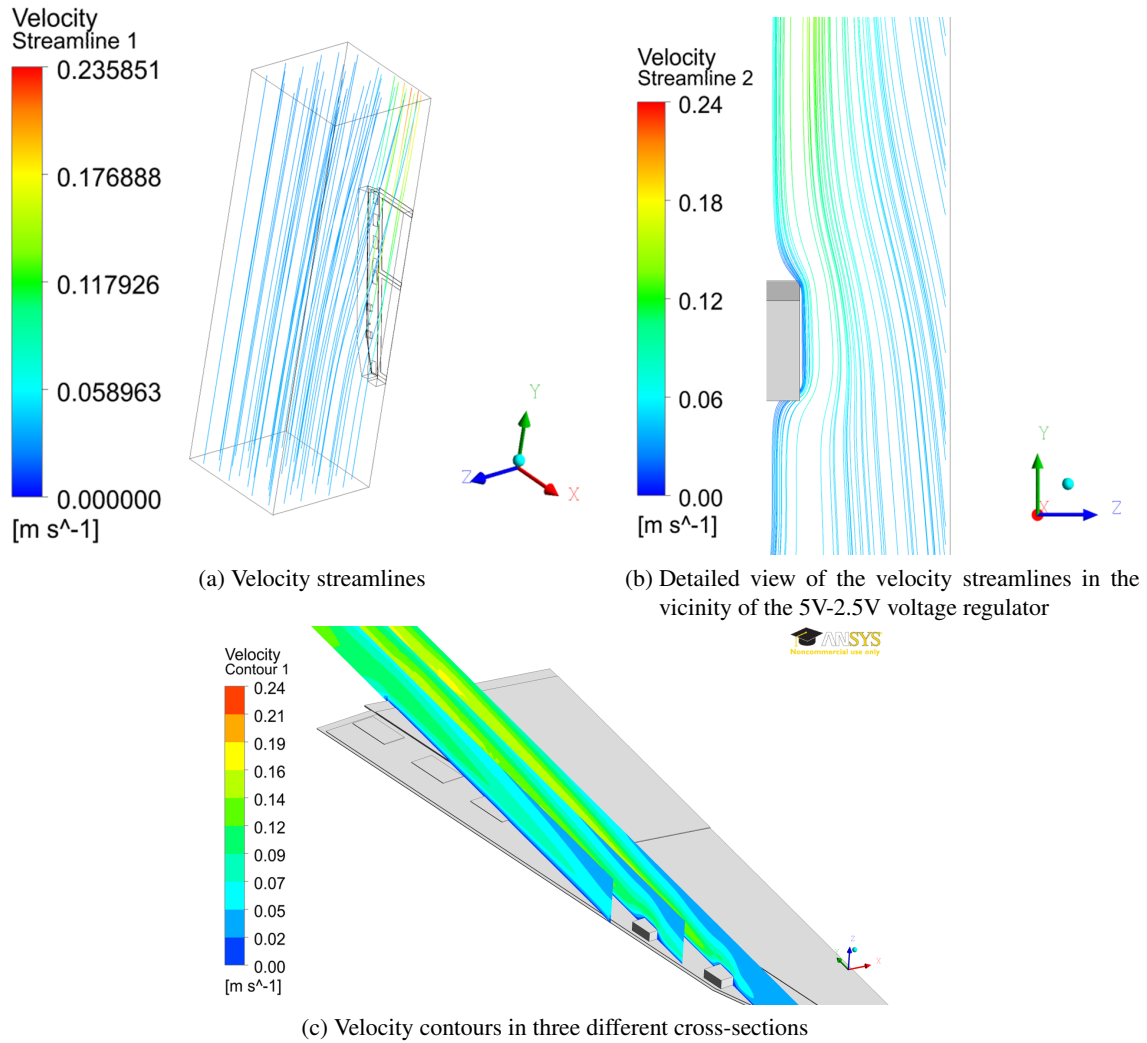


Figure 41: Air velocity in the vicinity of the ILC/ILD FTD petal.

As a result of this buoyancy driven flow, the petal is able to maintain overall temperatures below 40° C (see Figure 42). However, where the power dissipated is higher, hotspots appear in the petal, with peak temperatures achieving 67° C in the 5 V–2.5 V voltage regulator. Further studies will be needed to evaluate the ability of these components to withstand long-term exposure to these conditions. Furthermore, the impact of the high thermal gradients in the mechanical stability of the petal will also need to be assessed. It is important to note, however, that the model presented in this chapter only accounts for the cooling of a single petal. More detailed analyses will be needed for the cooling of a full disk. Nevertheless, the results presented indicate that it will be possible to cool a single ILC/ILD micro-strip FTD petal using natural convection

alone (as long as proper air renovation is provided to maintain the surrounding atmosphere at room temperature⁸⁾).

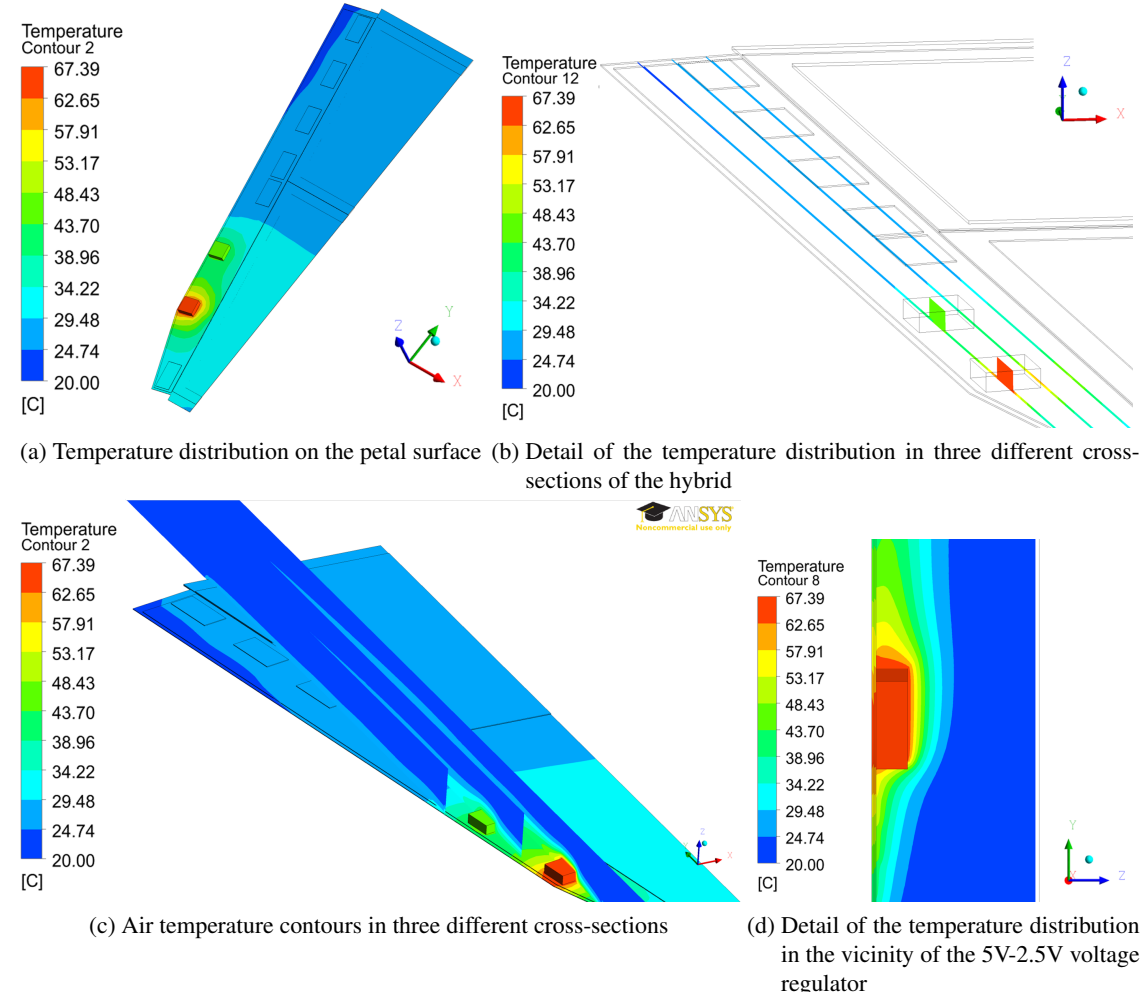


Figure 42: Temperature distribution in the ILC/ILD FTD petal.

⁸Taking as an example the volume between the FTD3 and FTD4 disks, the dissipated power is 16.75 W. For this power dissipation, a mass flow of 3.3 g/s entering and exiting the volume would be needed to assure that the average raise in air temperature be below 5 K.

2.6. Model Validation

In order to validate the CFD simulations presented in this note, the external flow of air over a flat plate has been simulated and the results compared with the analytical values available in literature.

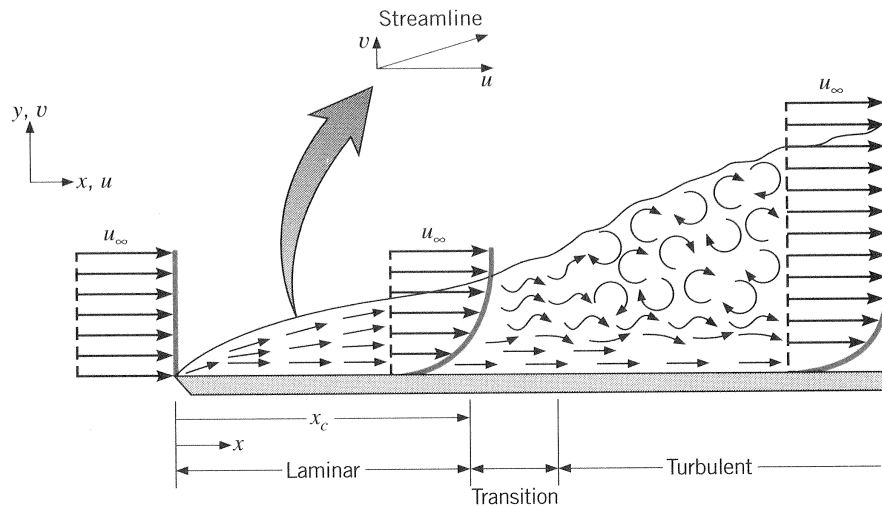


Figure 43: Velocity boundary layer development on an infinitely thin flat plate (from [8]).

A two-dimensional cross-sectional model has been created to replicate the problem shown in Figure 43. A rectangular, one cell deep, domain was drawn with the inlet ($v = 4 \text{ m/s}$ and $T = 0^\circ \text{ C}$) and outlet ($P_{rel} = 0 \text{ Pa}$) being defined along each of the domain's short edges respectively. The lower edge of the domain was split into two parts, with one being defined as a no-slip wall (that simulates the horizontal plate with a constant heat flux of 500 W/m^2) and symmetry boundary conditions applied to the other. In the upper edge of the domain, a symmetry boundary condition was also applied. The velocity contour for this domain and boundary conditions is shown in Figure 44. Its shape matched the theoretical one. In what concerns the temperature distribution over the plate, the results are shown in Figure 45. In the same Figure, the CFD results are overlaid on the analytical ones. For a horizontal flat plane in an external flow with a uniform surface heat flux being imposed, the following correlation for the laminar portion of the boundary layer (see Figure 43) can be applied:

$$Nu_x = \frac{h_x x}{k} = 0.453 Re_x^{1/2} Pr^{1/3} \quad (4)$$

which is valid for $Pr \geq 0.6$ and $Re_L \leq 5 \times 10^5$. In the correlation, Re_x and Nu_x are the Reynolds and Nusselt numbers respectively at a given distance x from the leading edge, h_x is the local convective heat transfer coefficient and k the fluid's thermal conductivity. For the problem at hand,

$Pr_{air} \approx 0.71$ and $Re_L \approx 8 \times 10^4$ which confirms the applicability of the correlation presented above. By performing an energy balance on the domain the following is also valid:

$$T_s(x) = T_\infty + \frac{q_s}{h_x} \quad (5)$$

where $T_s(x)$ is the plate's temperature at any given point, T_∞ is the bulk temperature of the air and q_s is the heat flux applied to the plate. From the combination of the two expressions above it is possible to calculate plate analytical temperature profile along its length (shown by the dotted line in Figure 45). As shown, the CFD results indicate a very good agreement with the analytical estimates, which validates the simulation.

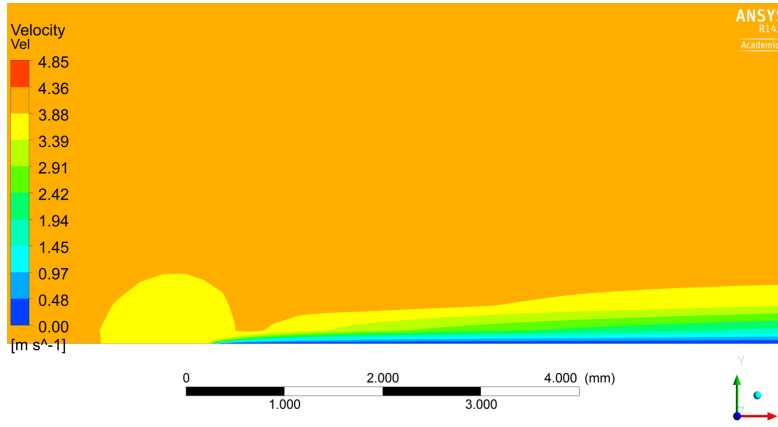
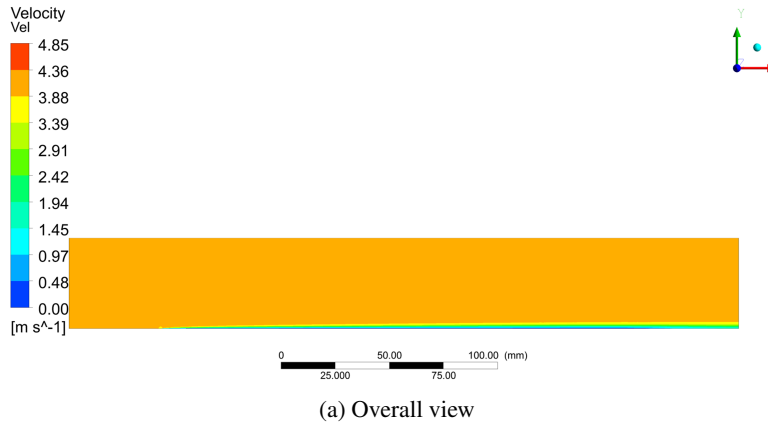


Figure 44: Velocity contour plot of the flow surrounding a flat plate in an external flow.

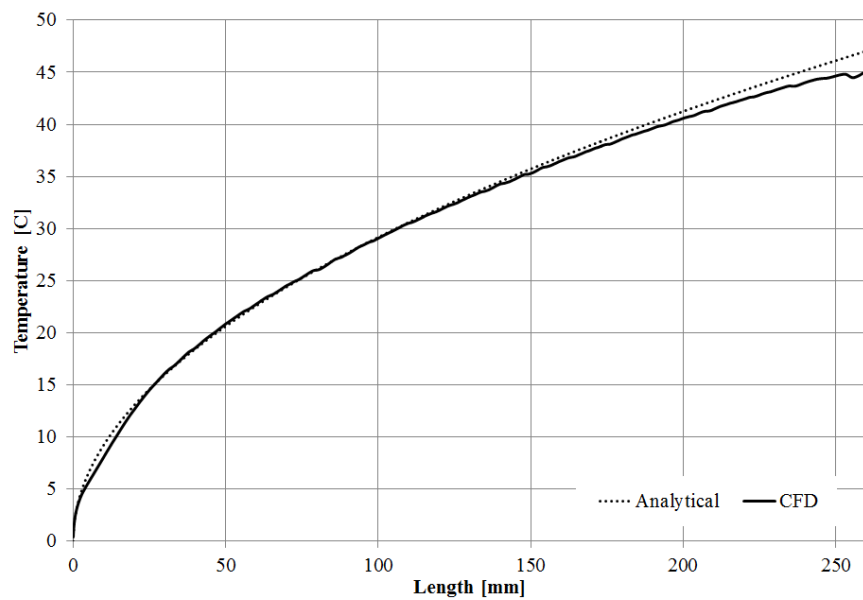


Figure 45: Comparison between analytical and CFD results for the temperature distribution over a flat plate in an external flow.

3. Conclusion

A cooling strategy for the inner detectors of the CLIC ILD detector concept was presented in this note. The use of a dry gas as a coolant is intended as a means to achieve the strict requirements in terms of material budget for the inner region. Therefore, forced convection is proposed for the cooling of the vertex detector, where the gas is delivered and extracted through a duct created by the addition of a stainless steel shield around the conical portions of the beam pipe. In order to cool both the vertex detector disks and barrel layers with a single stream, a proposal has been made to use a helical shaped flow in this region, with the associated changes to the geometry of the vertex detector endcap disks (the corresponding impact on the physics performance is currently under evaluation). First computational fluid dynamics simulations reveal the proposal's ability to properly cool the sensor surfaces, provided that the power dissipated remains relatively low (50 mW/cm^2). Nevertheless the current design requires further optimization in order to reduce the temperature gradient along sensor surfaces and between adjacent sensors. In the future, more detailed analyses will be needed to precisely quantify the achieved temperatures and their impact on the mechanical stability (namely temperature induced distortions) of the inner region. These analyses will require a more mature design of the sensors/readout chips, power consumption and support structures of the detectors. Furthermore, results validation through experimental measurements will also be required, as well as the evaluation of the air-induced vibrations on the support structures. Future work will focus on designing lightweight support structures that satisfy the material budget requirements and, at the same time, are able to withstand the static (due to pressure gradients) and dynamic (vibrations) forces caused by the air cooling system. Another area of future work is the evaluation of the impact of the temperature asymmetry (with respect to the x-y plane) inside the vertex detector on its overall physics and mechanical performance.

For what concerns the forward tracking detectors, the possibility of cooling with natural convection in an air atmosphere was evaluated for an ILC/ILD FTD silicon micro-strip petal. The results of the simulation show that, whilst the sensor temperature remains low, the temperature reached in the voltage regulators is relatively high (up to 67° C). The impact of these temperature values on the long term performance of such components remains to be evaluated. Furthermore, an analysis of the thermal-induced distortions of the petal will be needed, as well as the simulation of the cooling of a complete FTD.

A. CFD Model characteristics

In the creation and analysis of the models presented in this note, attention was paid to several parameters that govern the simulations. These parameters are introduced below.

A.1. Convergence criteria

In a CFD simulation convergence is reached when the following is achieved:

- Changes in solution variables from one iteration to the next are negligible (the residuals provide a mechanism to monitor this trend);
- Overall property conservation is achieved (the imbalances measure global conservation);
- Quantities of interest (e.g. temperature, pressure drop) have reached steady values.

A.1.1. Residuals

Residuals are a measure of how accurately the set of equations has been solved. In a CFD simulation, the continuous governing equations are discretized into a set of linear equations that can be solved. This set of equations can be written in the form:

$$[A][\Phi] = [b] \quad (6)$$

If the equations were solved exactly we would have:

$$[A][\Phi] - [b] = [0] \quad (7)$$

Since they are not, the residual vector $[R]$ is the error in the numerical solution and is given by:

$$[A][\Phi] - [b] = [R] \quad (8)$$

Since each control volume has a residual, a common practice is to take the root mean square (RMS) of the residuals as a convergence criteria. The RMS of the residuals is defined as:

$$RMS = \sqrt{\frac{\sum_i R_i^2}{n}} \quad (9)$$

A typical target for the convergence of a problem is to achieve a RMS of the residuals below 10^{-4} .

A.1.2. Imbalances

The global imbalances measure the overall conservation of a quantity (mass, momentum, energy) in the entire flow domain and they take the form:

$$\%Imbalance = \frac{FluxIn - FluxOut}{MaximumFlux} \cdot 100 \quad (10)$$

A target of less than 1% for the imbalances is a common practice.

A.1.3. Variables

In steady-state simulations another measure of the convergence of the solution is the stabilization of the quantities of interest. This is achieved by monitoring the evolution of these variables during the solution process.

A.2. Turbulence

In Computational Fluid Dynamics (CFD), turbulence models are used to predict the effects of turbulence in fluid flow without resolving all scales of the smallest turbulent fluctuations. Several models are available in ANSYS CFX to model the turbulence in the flow. The $k-\varepsilon$ model is the "industrial CFD" standard model since it offers a good compromise between the numerical effort and the computational accuracy. However this model has several known limitations related with the prediction of flow separation, swirling flows and flows with strong streamline curvature.

Another available model is the $k-\omega$ model which does not involve the complex non-linear damping functions required for the $k-\varepsilon$ variant and is therefore more accurate and robust.

The $k-\omega$ based Shear Stress Transport (SST) model accounts for the transport of the turbulent shear stress and gives highly accurate predictions of the onset and the amount of flow separation under adverse pressure gradients. Due to this ability for modelling flow separation, this model was chosen for the calculations presented in this note. Since this model does not use wall functions for the calculation of the near wall conditions a finer mesh in this area is needed when compared with the $k-\varepsilon$ model.

For the simulations mentioned in this note, the average Reynolds number is mentioned. This value is calculated by the software and uses as a characteristic length the cube root of the total volume and a velocity, density and viscosity from mass weighted averages in the domain. Its purpose is to verify if the assumption of a turbulent flow is applicable.

A.2.1. Near wall treatment

An important issue in turbulence modelling is the numerical treatment of the equations in regions close to walls. The near-wall formulation determines the accuracy of the wall shear stress and heat transfer predictions. Details about how this is accomplished in ANSYS CFX can be found in [9].

The variable y^+ is the dimensionless distance from the wall to the first node away from the wall. It is defined by:

$$y^+ = \frac{\sqrt{\frac{\tau_w}{\rho}} \cdot \Delta n}{\nu} \quad (11)$$

Where τ_w is the wall shear stress, ρ is the fluid's density, Δn is the distance between the first and second grid points off the wall and ν is the fluid's kinematic viscosity.

This variable is used to check the location of the first node away from a wall. If the value of y^+ is too large, then the wall function will impose wall type conditions further from the wall than would normally be physically appropriate. As a general guideline for the SST turbulence

model, the mesh should have a $y^+ < 2$ and a minimum of 15 nodes in the boundary layer (which has generally been respected in the models presented in this note).

A.3. Boundary Conditions

The typical boundary condition applied to the walls of the domains shown in this note is a no slip and smooth wall. By specifying a no slip boundary condition it is assumed that the fluid immediately next to the wall assumes the velocity of the wall, which is zero. This is the most common type of wall boundary condition implementation and it is the most appropriate for the models described in this note. The smooth wall boundary condition assumes that the wall surface has a zero roughness value. Although this is not fully applicable to the type of surfaces in the inner region, given the preliminary nature of the CFD simulations in this note, it is sufficient to assume that the wall roughness has a higher order impact in the obtained results. Future simulations will be needed to verify this assumption.

References

- [1] L. Linssen, A. Miyamoto, M. Stanitzki, and H. Weerts. Physics and Detectors at CLIC: CLIC Conceptual Design Report. (CERN-2012-003), 2012.
- [2] P. Roloff and N. Alipour Tehrani. Physics-performance optimization of the CLIC vertex detector. European Linear Collider Workshop ECFA LC2013, Hamburg, Germany, 2013.
- [3] N. Alipour Tehrani. Performance-Optimization Studies for the CLIC Vertex Detector. *École Polytechnique Fédérale de Lausanne*, 2013.
- [4] G. Blanchot and C. Fuentes. Power pulsing schemes for vertex detectors at CLIC. *Journal of Instrumentation*, vol. 8(01) p. C01057, 2013.
- [5] C. Fuentes. Power pulsing scheme based on a back-end current source for the analog electronics of the vertex detectors at CLIC. European Linear Collider Workshop ECFA LC2013, Hamburg, Germany, 2013.
- [6] A. Münnich and A. Sailer. The CLIC ILD_CDR Geometry for the CDR Monte Carlo Mass Production. (LCD-NOTE-2012-002), 2012.
- [7] T. Behnke, et al. International Linear Collider - Technical Design Report - Volume 3 - Physics and Detectors. 2012.
- [8] F. Incropera and D. DeWitt. *Fundamentals of heat and mass transfer*. John Wiley and Sons, 4th edn., 1996.
- [9] ANSYS CFX-Solver Modeling Guide. ANSYS, INC, 2012. Release 14.5.